# BUBBLE FORMATION DURING HORIZONTAL GAS INJECTION INTO DOWNWARD FLOWING LIQUID

Hua Bai and Brian G. Thomas

Hua Bai, former PhD student at UIUC, is now a senior research engineer with the Dow Chemical Company, 2301 N. Brazosport Blvd., Freeport, TX 77541. Brian G. Thomas is a Professor in the Department of Mechanical and Industrial Engineering, University of Illinois at Urbana-Champaign, 1206 West Green Street, Urbana, IL, 61801.

## ABSTRACT

Bubble formation during gas injection into turbulent downward flowing water is studied using high-speed videos and mathematical models. Bubble size is determined during the initial stages of injection and is very important to turbulent multiphase flow in molten metal processes. The effects of liquid velocity, gas injection flow rate, injection hole diameter, and gas composition on initial bubble formation behavior have been investigated. Specifically, bubble shape evolution, contact angles, size, size range and formation mode are measured. Bubble size is found to increase with increasing gas injection flow rate and decreasing liquid velocity, and is relatively independent of gas injection hole size and gas composition. Bubble formation occurs in one of four different modes, depending on liquid velocity and gas flow rate. Uniform-sized spherical bubbles form and detach from the gas injection hole in Mode I for low liquid speed and small gas flow rate. Modes III and IV occur for high velocity liquid flows where the injected gas

elongates down along the wall and breaks up into uneven sized bubbles. An analytical two-stage model is developed to predict the average bubble size, based on realistic force balances, and shows good agreement with measurements. Preliminary results of numerical simulations of bubble formation using a VOF model qualitatively match experimental observations, but more work is needed to reach a quantitative match. The analytical model is then used to estimate the size of the argon bubbles expected in liquid steel in tundish nozzles for conditions typical of continuous casting with a slide gate. The average argon bubble sizes generated in liquid steel are predicted to be larger than air bubbles in water for the same flow conditions. However, the differences lessen with increasing liquid velocity.

KEY WORDS: gas bubble formation, turbulent flow, steel continuous casting, slide-gate nozzle, argon gas injection, multi-phase flow, water modeling, CFD simulation.

## I. INTRODUCTION

Gas is injected into flowing liquid during many important processes. Bubbles form during the initial stages of gas injection, which govern their shape and size distribution. Bubble size is very important to subsequent turbulent flow phenomena for several reasons. In the processing of molten metals, argon gas is often injected to encourage liquid stirring, to help remove inclusions, and to help prevent reoxidation and clogging.

In the continuous casting of steel, for example, argon gas is injected horizontally through tiny holes on the inner wall of the nozzle, which connects the tundish and mold.

The injected gas encounters liquid steel flowing downward across its path. The downward liquid flow exerts a strong shear force on the forming bubble, which greatly affects its formation. If the gas stretches into a long sheet along the wall, the flow will behave very differently than if the gas stream simply breaks up into small bubbles that mix quickly with the liquid.

Knowing the bubble size is essential for studies of multiphase flow and related phenomena. The flow pattern in the continuous casting mold has been shown to depend on both the injection rate and the size of argon bubbles [1-3]. Furthermore, small bubbles can penetrate deep into the liquid pool and become entrapped by the solidified shell, causing quality problems, such as "pencil pipe" blister defects [4, 5]. Wang et al. [6] reported that an optimal bubble size exists for inclusion removal. Tabata et al. [7] performed water model tests to study the gas injection into the slide-gate nozzle, and found that large bubbles tended to move to the center of flow, thus lowering their ability to catch inclusions and to prevent their adherence to the nozzle wall.

This work was undertaken to increase understanding of the initial stages of bubble formation during horizontal gas injection into downward flowing liquid. Specifically, this work aims to quantify the bubble size as a function of important process parameters by first measuring air bubble size from injection into flowing water. Next, mathematical models are developed to accurately predict the bubble size measurements. Finally, the model is applied to estimate the size of bubbles expected during argon injection into flowing steel under conditions typically encountered in tundish nozzles used in the continuous casting of steel.

## II. PREVIOUS WORK

Previous work on bubble formation in liquid metals includes a few experimental studies on gas-stirred vessels with gas injected from an upward-facing orifices or tubes submerged in relatively quiescent liquid. The frequency of bubble formation was measured by using pressure pulse [8, 9], resistance probe [10, 11], or acoustic devices [12]. The mean bubble volume and the corresponding equivalent diameter are then derived from the known gas injection flow rate and the frequency of bubble formation. Efforts to directly observe bubble formation in liquid metal have been made using X-ray photography [13, 14].

Few theoretical modeling studies have been reported for bubble formation in metallic systems. Guthrie and coworkers calculate that bubbles injected vertically into stagnant metallic systems are bigger than air bubbles in water [15].

Extensive studies of bubble formation have been done on aqueous systems, both experimentally and theoretically, as reviewed by Kumar and Kuloor [16], Clift et al. [17], Tsuge [18], and Rabiger and Vogelpohl [19]. Recently, Wang et al [20] used water models to study air bubble formation from gas injected through porous refractory into an acrylic tube with flowing water. Wettability was reduced by waxing the nozzle walls, which caused the gas to form a large curtain traveling along the wall, which broke into many uneven-sized bubbles. On an unwaxed surface, uniform-sized bubbles formed and detached from the wall to join the liquid flow.

Most previous studies modeled bubble formation in stagnant liquids. The theoretical studies fall into two categories: analytical models of spherical bubbles and discretized models of non-spherical bubbles. The spherical bubble models solve a force

balance equation and/or bubble motion equation for the size of the growing spherical bubble at detachment. Forces are evaluated for the entire growing bubble. Two of many significant contributions are the single-stage model of Davidson and Schuler [21] and the two-stage model of Kumar and Kuloor [22]. These models adopt empirical criteria to determine the instant of detachment.

In contrast, non-spherical bubble models have been developed [23-26] that are based on a local balance of pressure and force at the gas/liquid interface. In these models, the bubble surface is divided into many two-dimensional axisymmetric elements. For each element, equations of motion in both the radial direction and vertical directions are solved for the radial and vertical velocities, which are used to find the position of each element. The bubble growth and bubble detachment is determined by calculating the (non-spherical) shape of the bubble during its formation. These models have the advantage that empirical detachment criteria are not required. Unfortunately, they are not applicable to non-axisymmetric conditions such as arise with shearing flowing liquid. Even full numerical simulation of bubble formation was reported by Hong et al., [27] who modeled the formation of a bubble chain in stagnant liquid by tracking the movement of the discretized gas-liquid interface using the VOF (Volume of Fluid) method in CFD. [28]

Only a few studies [29-31] have modeled bubble formation with flowing liquid. In these models, the analytical models of spherical bubble formation in a stagnant liquid are modified to accommodate uniform liquid flow by adding a drag force due to the flowing liquid in the equation of motion. More empirical parameters are introduced in order to match experimental results, so these models are limited to the particular systems and conditions of the measurements.

## III. WATER MODEL EXPERIMENTS

Water model experiments are performed to investigate bubble formation during gas injection through tiny horizontal pores into turbulent liquid flowing vertically down the wall. This shears the growing bubbles from the wall under flow conditions that incorporate the essential phenomena in tundish nozzle flow. High-speed video photography is used to visualize the effects of liquid velocity, gas injection flow rate, gas injection hole size, and gas composition on the bubble size, shape, frequency, mode, and size distribution. In addition to quantifying these important parameters, the results of these water experiments also serve to validate the theoretical model developed later.

### *A. Experimental apparatus and procedure*

Figure 1 shows a schematic of the experimental apparatus. Water flows down from an upper tank that simulates a tundish, through a vertical tube that simulates a tundish nozzle, and into a tank at the bottom that simulates a casting mold. The vertical tube is 600 mm long Plexiglas with a square 35 x 35 mm cross section. The gas (air, helium, or argon) is injected through a plastic tube attached to a hollow needle inserted horizontally into the square tube, 220 mm below the tundish tank outlet. The needle outlet is aligned flush with the nozzle wall to simulate a pierced hole on the inner wall of a nozzle. Three different-sized needle hole sizes are used to examine the effect of the gas injection hole diameter (0.2, 0.3, and 0.4 mm). The gas flow controller is adjusted to achieve volumetric gas flow rates of 0.17 - 6.0 ml/s per orifice, using an orifice meter located about 1 m from the needle. These flow rates correspond to 0.67 – 19.3 % gas (0.34 – 12.0 SLPM) of argon gas injection into 1500 ˚C molten steel cast at $4.473 \times 10^{-3}$

$m^3/s$ through a typical nozzle with 140 drilled holes (or 140 active sites in a porous refractory). Water flow rate is adjusted to approximate conditions in a tundish nozzle by partially blocking the bottom of the nozzle. The average water velocity varies from 0.6 to 3.1 m/s, which corresponds to pipe Reynolds numbers of 21,000 - 109,000. The water velocity is obtained by measuring from the video frames, the average speed of tracer particles which are added to the water.

The formation of bubbles is recorded by a video camera at 4500 frames per second. Each recorded sequence contains 1000 frame images taken over 0.22 second. This high speed was necessary to capture the rapid events that occur during bubble formation. The vertical head of liquid, from the top surface of the liquid in the upper tank to the needle, is about 500mm and drops less than 20mm during video recording, owing to the short measurement time.

The behavior of bubbles exiting from the needle hole is studied by inspecting the sequences of video images frame by frame. The frequency ($f$) of bubble formation is determined by counting the number of the bubbles generated at the exit of the injection hole during the recorded time period. The mean bubble volume ($V_b$) is then easily converted from the known gas injection volumetric flow rate ($Q_g$), via

$$V_b = \frac{Q_g}{f} \tag{1}$$

An equivalent average bubble diameter ($D$) is calculated assuming a spherical bubble, or

$$D = \left( \frac{6Q_g}{\pi f} \right)^{1/3} \tag{2}$$

Bubbles sizes are also measured directly from individual video images in order to validate this procedure and to check the bubble size deviation from its average value. In some tests, a second needle is inserted into the nozzle wall 12.5mm downstream below

the first needle in order to study the interaction between bubbles from adjacent gas injection sites.

*B. Bubble size in stagnant liquid*

Experiments are first performed with stagnant water where previous measurements and models are available for comparison. This was accomplished simply by keeping the bottom of the tube closed. Although most previous studies are based on bubble formation from an upward facing orifice or nozzle, some authors [12, 16] observed that bubbles formed from a horizontal orifice behaved almost the same as in stagnant liquid. Figure 2 shows the measured bubble diameters together with a prediction using Iguchi's empirical correlation [14]. Iguchi's equation is a curve fit of bubble sizes measured at relatively large gas flow rates of 20 - 413 ml/s per orifice injected vertically into stagnant liquid. The agreement is reasonably good, which confirms that this equation also applies to horizontal injection at the relatively low gas flow rates of this work.

The results in Figure 2 show that bubble size increases with increasing gas injection flow rate. For the same gas injection rate, a bigger injection orifice produces larger bubbles. At high gas injection rates, larger bubbles emerge from larger diameter orifices. However, orifice size becomes less important at small gas injection rates.

*C. Bubble size in flowing liquid*

Experiments are next performed with gas injected into flowing water. The measured mean bubble sizes are plotted in Figure 3. Each point in Figure 3 represents the mean bubble diameter obtained from the measured frequency using Eqs. (1) and (2) for a single test with a particular gas injection flow rate, water velocity and gas injection

hole size. In addition, the maximum and minimum bubble sizes were obtained by directly measuring the video images for each test. This range of bubble sizes is shown as "error bars" for each point. Also shown on the figure is the symbol (circle, triangle or square) representing the corresponding bubble formation mode that is discussed in section D.

Figure 3 shows that the mean bubble size increases with increasing gas flow rate and decreasing water velocity. Comparing Figures 2 and 3, it can be seen that at the same gas injection flow rate, the bubble size in flowing liquid is much smaller than in stagnant liquid. This becomes much clearer when the volumes of bubbles formed in stagnant and flowing liquid are plotted together, as shown in Figure 4. The bubble volumes formed in flowing water are 5 to 8 times smaller than those in stagnant water.

Physically, the smaller bubble size in flowing liquid is natural because the drag force from the liquid flow along the wall acts to shear the bubbles away from the tip of the gas injection hole into the liquid stream before they have time to grow to the mature sizes found in stagnant liquid. Moreover, Figure 3 also shows clearly that for a given gas flow rate, the higher the velocity of the shearing liquid flow, the smaller are the detached bubble sizes.

The combined effects of gas injection rate, liquid velocity and gas composition on bubble volume are shown together in Figure 5. The trends are identical to those in Figure 3, except that the differences in bubble volume are magnified relative to those in diameter. All of the experimental data shown in Figures 2-4 are for air. Further experiments with argon and helium investigated the effect of gas compositions. Figure 5 shows that the measured mean bubble sizes for three different gases (air, argon and

helium) are all about the same. Thus, the gas composition has little influence on bubble size, at least for the conditions studied here.

It appears that bubble size is relatively independent of gas injection hole size. This can be seen by comparing Figures 3(a), (b) and (c). This observation is different from that in stagnant liquid, where bubble size is slightly larger for larger injection holes. This suggests that the shearing force due to the flowing liquid dominates over other effects related to the hole size such as the surface tension force.

Figures 2-5 show that the data collected with higher water velocities generally also tend to have higher gas flows. This choice of test conditions was an unplanned consequence of the greater water flow inducing lower pressure at the orifice, which consequently increased gas flow rate. The higher-speed flowing liquid acts to aspirate more gas into the nozzle. This observation illustrates the important relationship between liquid pressure and gas flow rate that should be considered when investigating real systems.

*D. Bubble formation mode*

The initial shape of the bubble growing and exiting the gas injection hole was observed to behave in one of four distinct modes, shown in the representative recorded images of Figure 6. Figure 7 shows sequences of recorded images for two tests which illustrate two of these modes. The detailed stages of bubble formation are illustrated more clearly by tracing these images, as shown in Figure 8.

Figure 6 shows close-up photos of bubbles exiting pairs of injection holes for each mode. The upper four frames show side views, including the nozzle wall (right). This view is complicated by the dark portion of the nozzle wall where the needle is

inserted, and by the edges of plastic supports, which are both outside of the model and have no influence on the flow. The lower frames in Figure 6 show the perpendicular end views for three modes, looking at the nozzle wall into the injection hole (all same scale). Schematic tracings of two dark photos are included for clarity.

For low velocity water flows (less than 1m/s) and small gas injection rates (less than 2ml/s), Mode I is observed. In this mode, uniform-sized spherical bubbles form at the tip of the gas injection hole, as shown in Figures 6 (a), (e) and (f). Each bubble elongates slightly before it discretely detaches from the hole and joins the liquid stream, as a spherical bubble again. This sequence of events is shown in ten steps in Figures 7(a) and 8(a). The entire process needs only 0.004s for these conditions. For this mode, no interaction was observed between bubbles flowing from the upper injection hole and those from the lower hole, when it was there. It is expected that such independent behavior of the bubbles would be observed even for gas flow through porous refractories, where the individual pores which actively emit bubbles might be spaced closer together. Thus, mode I corresponds to bubbly flow.

At the other extreme, Mode IV is observed for high velocity water flows (more than 1.6m/s) and very large gas injection rates (more than 10ml/s). In this mode, each bubble elongates down along the wall and forms a sheet or curtain. This curtain merges with the gas from the lower hole, if it exists, to form a long, wide continuous gas curtain. Both the thickness and width of the curtain increase with distance below the injection hole, as shown in Figures 6 (d) and (i). This is due to the gradual decrease in downward gas velocity, as the buoyancy forces increase. This mode likely leads to the detrimental "annular" flow condition, where the gas and liquid phases separate into large fluctuating

regions [32]. The curtain eventually becomes unstable when its thickness becomes too great and it breaks up into many bubbles with different sizes. Their sizes range from a few that are very large to others that are very tiny. For the range of gas flow rates of practical interest to gas injection into steel nozzles, (less than 3.5 ml/s per orifice), this regime is not expected.

Mode III is observed for conditions of high water velocity (more than 1.6m/s) and for gas injection flow rates typical of steel casting (less than 6ml/s). Mode III is similar to Mode IV except that there is insufficient gas flow to maintain a continuous gas curtain, so gaps form. Before detaching from the gas injection hole, Figures 7(b) and 8 (b) document how the bubbles in this mode simultaneously expand and elongate to reach almost twice their diameter by the instant of detachment. The bubbles continue to elongate as they move down along the wall. They remain against the wall for some distance below the injection hole before moving off to join the general flow. When a second (lower) injection hole exists, the two bubble streams often coalesce to form larger elongated bubbles. This further contributes to the non-uniform size distribution. Figures 6 (c), (g) and (h) show the ellipsoidal shape of bubbles resulting from this mode.

Mode II is a transitional mode between Modes I and III in which the injected gas initially elongates along the wall but quickly detaches from it. When two gas injection holes are used, the bubbles from the upper hole do not coalesce with bubbles from the lower hole for cases classified as Mode II. Bubbles sizes for Mode II are still relatively uniform compared to those in Modes III and IV.

*E. Mode and size range*

In addition to the measured mean bubble size, Figure 3 also shows the mode and the bubble size range, represented by error bars. Higher liquid velocities keep the bubbles closer to the wall. Higher gas flows tend to make the gas stream continuous. All cases with water velocity of 0.9m/s or less fall into Mode I and have a very tight size distribution, which corresponds to relatively uniform spherical bubbles detaching near the tip of the hole. Most of the cases in Figure 3 with a water velocity about 1.4m/s fall into Mode II and have slightly wider size ranges. All cases with liquid velocity of 1.9m/s or more fall into either Mode III or Mode IV, and have huge size ranges, which corresponds to the break-up of a discontinuous gas curtain into uneven-sized bubbles. Bubble diameters as small as 0.5mm are measured. The continuous gas curtain in Mode IV is observed only at very high gas flow rates, ($Q_g$ > 10 ml/s per hole), not shown in the plots.

*F. Bubble elongation measurement*

The bubble is observed to grow and elongate during its formation. To quantify the bubble shape during this process, the vertical elongation length of the bubble ($L$) is measured at the instant of detachment of the bubble from its injection hole, as shown in Figure 9(a). The measured bubble elongation lengths are plotted for different gas flow rates and liquid velocities in Figure 9(b). The effects become more clear when plotting the elongation factor, $e_d$, defined as the ratio of the elongation length ($L$) and the equivalent bubble diameter ($D_d$) (defined using Eqs. (1) and (2) which assume a spherical bubble with the same volume)

$$e_d = \frac{L}{D_d} \tag{3}$$

As shown in Figure 10(a), the elongation factor varies from 1.3 to 1.8 and depends mainly on the liquid velocity. It is relatively independent of the gas injection flow rate. Bubbles elongate slightly more at higher liquid velocity. Figure 10(b) illustrates this effect of liquid velocity, $U$, on the measured average elongation factors. These four data points are well fitted with a simple quadratic function,

$$e_d = 0.78592 + 0.70797U(m/s) - 0.12793U(m/s)^2 \quad (4)$$

*G. Contact angle measurement*

Contact angles were measured from the bubble photographs in this work in order to better evaluate the surface tension forces acting on the bubble. The surface tension forces depend on the contact angles between the bubble and the wall as follows [33],

$$F_{Sz} = \frac{\pi}{2} r \sigma f_\theta \quad (5)$$

where the contact angle function, $f_\theta$, depends on the static contact angle, $\theta_0$, and the difference between the contact angles above and below the bubble,

$$f_\theta = \sin\theta_o \left(\cos\theta_r - \cos\theta_a\right) \quad (6)$$

The static contact angle is defined by the profile adopted by a liquid drop at rest on a flat horizontal surface and was measured to be 50° for the current water / air / solid-plastic system. The flowing liquid alters the contact angle around the interface circumference, as shown in Figure 11(a). Stretching of the upstream edge of the bubble increases the contact angle, defined there as the advancing contact angle, $\theta_a$. Compressing of the downstream edge of the bubble decreases the contact angle, defined there as the receding contact angle, $\theta_r$.

Table I shows the mean contact angles measured in the water experiments with an uncertainty of +/- 5˚. With increasing liquid velocity, the advancing contact angle $\theta_a$ increases, and the receding contact angle $\theta_r$ decreases. The effect of gas flow rate is relatively small. The contact angle function $f_\theta$ increases with increasing liquid velocity, as plotted in Figure 12. The four data points are well fitted with a simple quadratic function,

$$f_\theta(U) = -0.06079 + 0.33109U(m/s) + 0.078773U(m/s)^2 \qquad (7)$$

## IV. ANALYTICAL MODEL FOR BUBBLE SIZE PREDICTION

The formation of bubbles during horizontal gas injection into vertical fast-flowing liquid is very different from the classic bubble formation problem of vertical gas injection into stagnant liquid, studied with many previous models. When horizontally-injected gas encounters severe downward shearing forces, smaller bubbles result, as documented by the measurements in the previous section. Unlike bubble formation in stagnant liquid, in which buoyancy is the major driving force for bubble detachment, the buoyancy force here acts to resist bubble detachment against the drag force of downward liquid momentum. Thus, a new analytical model had to be developed, based on balancing the forces acting on the growing bubble and setting a proper bubble detachment criterion.

### *A. Forces acting on a growing bubble*

Correct evaluation of the fundamental forces acting on the growing bubble is essential for an accurate analytical model of bubble formation that can be extrapolated to other systems. A schematic of the fundamental forces acting on a growing bubble is

shown in Figure 13. The forces of liquid drag, buoyancy, and surface tension are now discussed in turn.

Drag force due to flowing liquid $F_D$

The liquid flowing down the wall exerts a downward drag force on the growing bubble, $F_D$, which depends on the exact nature of the steep liquid velocity profile near the wall. A reasonable and convenient equation describing the velocity profile for fully developed turbulent flow in a pipe, is the seventh root law profile [34]

$$u = 1.235U\left(\frac{y}{D_N / 2}\right)^{1/7} \tag{8}$$

where y is the distance from the wall, $D_N$ is the nozzle diameter, and $U$ is the mean vertical liquid velocity in the nozzle. The steady average liquid velocity across the growing bubble, $\bar{u}$, depends on the instantaneous bubble size and is estimated from

$$\bar{u} = \frac{1}{2r}\int_{y=0}^{y=2r} u dy = 1.3173U\frac{r^{1/7}}{D_N^{1/7}} \tag{9}$$

where $r$ is the equivalent horizontal radius of the forming bubble. The drag force acting on the growing bubble, $F_D$, is

$$F_D = C_D\frac{1}{2}\rho_l\bar{u}^2\pi r^2 \tag{10}$$

Assuming the bubble Reynolds number, $Re_{bub}$, is less than $3\times10^5$, the drag coefficient $C_D$ is [17]

$$C_D = \frac{24}{\mathrm{Re}_{bub}}(1+0.15\,\mathrm{Re}_{bub}{}^{0.687}) + 0.42/(1+4.25\times10^4\,\mathrm{Re}_{bub}^{-1.16}) \tag{11}$$

where $Re_{bub}$ is defined by

$$Re_{bub} = \frac{\bar{u}D}{\upsilon} \tag{12}$$

where $D$ is the equivalent bubble diameter and υ is the kinematic viscosity of the liquid. This downward drag force naturally increases as the bubble grows and extends into faster moving fluid.

Buoyancy force $F_B$

The upward buoyancy force of the low density gas acts to resist the drag force of the liquid momentum. This force increases simply and dramatically with increasing bubble diameter:

$$F_B = V_b(\rho_l - \rho_g)g = \frac{1}{6}\pi D^3(\rho_l - \rho_g)g \qquad (13)$$

Surface tension force $F_S$

A surface tension force arises when the bubble deforms and its upper and lower contact angles differ, according to Eq. (5) as discussed earlier. The vertical component of this force acts upward to resist the downward drag and keep the bubble attached to the gas injection hole. It increases as the bubble grows because of both the increasing bubble radius and the increasing deformation of the bubble as its shape elongates.

*B. Two-stage model for bubble formation*

The relative increases of the three fundamental forces acting on the bubble as it grows are compared in Figure 14, based on the equations just presented. Other forces, such as the inertial force due to the rate of change of momentum of the growing bubble, are believed to be negligible so were neglected. A two-stage model is developed to predict the size of the bubbles formed by balancing these forces and then applying a reasonable detachment criterion. Bubble formation is assumed take place in two idealized stages, the expansion stage and the elongation stage, as shown in Figure 15.

Expansion stage

During the expansion stage, the bubble expands while holding onto the tip of the gas injection hole. This stage is assumed to end when the downward force is first able to balance the upward forces. That is,

$$F_D = F_B + F_{Sz} \tag{14}$$

The shape of the bubble during this stage is not considered until at the instant of the force balance when it is assumed to be spherical. Substituting Eqs. (5), (10) and (13) into Eq. (14) yields

$$C_D \frac{1}{2}\rho_l \bar{u}^2 \pi r^2 = \frac{4}{3}\pi r^3(\rho_l - \rho_g)g + \frac{1}{2}\pi r\sigma \sin\theta_O(\cos\theta_r - \cos\theta_a) \tag{15}$$

In Eq. (15), $\bar{u}$ depends on $r$, which is the unknown. Thus, Eqs. (9) and (15) are solved simultaneously for $r$ by trial and error to yield $r_e$, which is the equivalent radius of the bubble at the end of the expansion stage.

Elongation stage

As the bubble continues to grow, the downward force eventually exceeds the upward forces acting on the bubble. This makes the growing bubble begin to move downward along with the liquid flow. The bubble keeps expanding since it still connects to the gas injection hole, and at the same time it elongates due to the shearing effect of the liquid flow.

During this elongation stage, the shape of the bubble is idealized as an ellipsoid. It is assumed to connect with the injection hole through a thin neck with negligible volume. The two horizontal radii of the ellipsoid, in the x and y directions, are assumed to be equal to $r$ for simplicity.

The vertical radius of the ellipsoid ($r_z$) incorporates bubble elongation and is related to the equivalent bubble diameter ($D$) and the elongation factor ($e$) by

$$r_z = \frac{1}{2} eD \tag{16}$$

The volume of the ellipsoidal bubble is equated to an equivalent diameter spherical bubble ($D$),

$$\frac{4}{3}\pi\, r^2 r_z = \frac{1}{6}\pi D^3 \tag{17}$$

The instantaneous equivalent diameter ($D$) of the bubble is related to the instantaneous horizontal radius ($r$) of the ellipsoid and the instantaneous elongation factor ($e$) by rearranging Eqs. (16) and (17):

$$D = 2r\sqrt{e} \tag{18}$$

The bubble elongates more as it grows. The bottom of the ellipsoidal bubble is assumed to travel with the liquid at the average velocity $\bar{u}$, defined in Eq. (9). The criterion to end this second stage of bubble growth is when the bubble elongates to the measured elongation at detachment from the gas injection hole, defined by $e_d$. This critical length of the bubble at the instant of detachment is related to the time needed for the fluid to travel from point A to B in Figure 15 (b).

$$\int_{t_e}^{t_d} \bar{u}\,dt = e_d D_d + \frac{d}{2} - r_e \tag{19}$$

where times $t_e$ and $t_d$ indicate the end of the expansion stage and the instant of bubble detachment respectively. $r_d$ is the horizontal radius at detachment.

The time during bubble growth ($t$) is related to the instantaneous horizontal radius of the growing ellipsoidal bubble ($r$) by volume conservation, which assumes that

pressure and temperature inside the growing bubble are sufficiently constant to avoid compressibility effects.

$$Q_g t = \frac{1}{6}\pi D^3 \tag{20}$$

Assuming that the bubble elongates linearly from 1 (spherical bubble at $t_e$) to $e_d$ (detachment at $t_d$), the elongation factor evolves according to:

$$e = ar + b \qquad at \quad r_e \le r \le r_d \tag{21}$$

where the constants $a$ and $b$ are:

$$a = \frac{e_d - 1}{r_d - r_e} \tag{22}$$

$$b = \frac{r_d - e_d r_e}{r_d - r_e} \tag{23}$$

Inserting Eqs. (18) and (21) into Eq. (20) and differentiating gives,

$$dt = d\left(\frac{4\pi}{3Q_g} r^3 e^{3/2}\right) = \frac{4\pi}{Q_g}\left(r^2(ar+b)^{3/2} + \frac{ar^3}{2}(ar+b)^{1/2}\right)dr \tag{24}$$

Substituting Eqs. (9), (18) and (24) into Eq. (19) yields the final model,

$$5.2692\frac{\pi U}{Q_g D_N^{1/7}}\int_{r_e}^{r_d}\left(r^{15/7}(ar+b)^{3/2} + \frac{ar^{22/7}}{2}(ar+b)^{1/2}\right)dr = 2r_d e_d^{3/2} + \frac{d}{2} - r_e \tag{25}$$

Eq. (25) is solved for the horizontal radius of the ellipsoidal bubble at the instant of detachment from the gas injection hole, $r_d$, which is the only unknown in this equation, using trial and error iteration with a program written in MATLAB detailed elsewhere [35]. The equivalent bubble diameter at detachment is then found by inserting $r_d$ and $e_d$ into Eq. (18).

It should be noted that there are no adjustable parameters in this model. The elongation factor at the instant of the bubble detachment ($e_d$) and the contact angle function ($f_\theta$) depend on the mean liquid velocity ($U$), and are based directly on the experimental measurements, using empirical Eqs. (4) and (7) in the model.

## V. COMPARISON OF MODEL PREDICTIONS AND MEASUREMENTS

The bubble diameters predicted by the two-stage model are shown in Figure 16, together with the measured mean bubble diameters. The fluid properties and operating conditions used in the calculation are given in Table II.

Figure 16 shows that the match between the model prediction and the experimental data is reasonably good, although the bubble diameter appears to be slightly over-predicted at low gas injection rates. This agreement is remarkable considering the crude assumptions regarding bubble shape and the lack of calibration parameters in the model.

The model and experimental results in Figure 16 show the same trends for the effects of the liquid velocity and gas flow rate. Specifically, the mean bubble size increases with increasing gas injection flow rate and decreasing liquid velocity.

The model predicts that the gas injection hole size has little effect on the bubble size at high liquid velocity ($U \geq 1.4$m/s). This is consistent with the water experiments, where it is difficult to distinguish between data measured from different hole sizes. However, at low liquid velocity, ($U \leq 0.9$m/s), the influence of the hole size increases, as shown in Figure 16 (a) and the larger gas injection hole generates slightly larger bubbles. This trend suggests a smooth transition from the behavior observed in stagnant liquid,

where gas injection hole size is very important, to the high liquid velocities in Figures 16(b)-(d).

The analytical model also predicts a negligible effect of the gas density that again matches the experimental measurements. The gas density only appears together with the liquid density in the $(\rho_l-\rho_g)$ term of Eq. (15), where it is clearly negligible.

## VI. NUMERICAL MODEL

The analytical two-stage model conveniently and accurately predicts the average bubble size in the system of interest in this study. It does not predict other important gas bubble behavior such as bubble formation mode, bubble shape, bubble size deviation, bubble coalescence and break-up, and the interaction between the bubbles and the liquid flow. Direct numerical simulation of bubble formation is a potential method to overcome this limitation.

The Volume of Fluid (VOF) method, developed by Nichols and Hirt [28] is well suited to model the flow of liquid coupled with the movement of a gas-liquid interface by solving local-instantaneous conservation equations and boundary conditions. This method employs an algorithm to track the free surface moving through a computational grid. Previous simulation of a single bubble chain in stagnant liquid using this VOF method has been reported [27] to agree well with the experimental results in a real time sequence. The method was applied here to simulate bubble formation during the horizontal injection of gas into vertical water flow measured in this work.

*A. VOF Model Description*

In this VOF method, differential conservation equations are solved only in the liquid phase. The gas-liquid interface, which forms the bubble surface, is treated as a movable pressure boundary. It appears reasonable to assume a uniform pressure inside each bubble. Furthermore, neglecting gas momentum and motion of the gas inside the bubble would also appear to be reasonable for a gas-liquid flow system, where the liquid density is 3 to 4 orders of magnitude higher than that of the gas. By tracking the arbitrary shape which the gas-liquid interface can attain, the evolution of bubble shape can be realistically simulated.

In addition to solving the differential equations for the conservation of mass and momentum in the liquid phase, the position of the gas-liquid interface is defined by solving for the liquid volume fraction ($f$). This function equals one in a pure liquid region, and is zero in a pure gas region. Accordingly, $f$ lies between 1 and 0 in any cell which contains a gas-liquid interface. From the mass conservation of the liquid phase, the time-dependent governing equation for $f$ is

$$\frac{\partial f}{\partial t} + \frac{\partial (v_i f)}{\partial x_i} = 0 \tag{26}$$

The local curvature of the bubble surface, defined by the radius of curvature $R$, is related to the pressure difference across the gas-liquid boundary according to the Laplace-Young equation [36]

$$P_b - P = \frac{2\sigma}{R} \tag{27}$$

where $P_b$ is the pressure in the bubble and $P$ is the pressure of the liquid phase.

Pressure in the bubble is defined differently for growing and isolated bubbles. A growing bubble that is still attached to the gas injection hole has a gas source with a constant gas flow rate being injected. This bubble is assumed to be adiabatic, so the pressure inside the growing bubble ($P_b$) is related to its volume ($V_b$) by

$$V_b \frac{dP_b}{dt} + \gamma P_b \frac{dV_b}{dt} = \gamma P_g Q_g \tag{28}$$

where $\gamma$ is the ratio of the specific heats of the gas, $Q_g$ is the gas injection flow rate.

Bubbles that have detached from the injection hole are isolated from the gas source. In these bubbles, the pressure is related to volume by

$$P_b V_b^{\gamma} = constant \tag{29}$$

The standard, two-equation $K$-$\varepsilon$ turbulence model is chosen to model turbulence, which requires the solution of two additional transport equations to find the turbulent kinetic energy, $K$, and the turbulent dissipation, $\varepsilon$, fields [37]. The liquid phase mass and momentum conservation equations, $K$-$\varepsilon$ equations, and Eqs. (26)-(29) are discretized using the finite difference method and solved with the FLOW-3D v7.1 code developed by Flow Science, Inc. [38].

*B. Preliminary results*

A sequence of air bubble formation profiles is shown in Figure 17 for a numerical simulation of a typical experimental condition, with 2ml/s air flow rate injected horizontally from a 0.3mm hole into water flowing downward at 1m/s. The 3-D computational domain (5.3mm x 2mm x 4.6mm) simulates a small part of the liquid flow region near the gas injection hole for one symmetric half of the bubble.

The simulated bubble formation sequence qualitatively matches the experimental observations for this mode I case. The bubbles elongate slightly during the forming process. After disconnecting from the gas injection hole, the bubbles travel along the wall for a short distance before they detach from the wall and become spherical. Although this behavior matches the observations qualitatively, the quantitative match is not as good. The equivalent diameter of the simulated bubble (~ 0.6mm) is much smaller than the measurement (2.0mm) and the analytical model prediction (1.96mm). Many factors might contribute to this discrepancy, such as the boundary layer model (wall law), inlet conditions, constant gas flow rate assumption, uniform gas pressure assumption, and numerical problems. Further work is needed to obtain more quantitative numerical simulations of bubble formation.

## VII. ARGON BUBBLE SIZES IN LIQUID STEEL

The size of argon bubbles injected into refractory tundish nozzles is important to clogging and flow behavior in the continuous casting of steel. Owing to its accuracy in matching the water-air experiments and its fundamental basis, the analytical two-stage model was applied to estimate the initial size of argon bubbles expected in molten steel in this process. Despite the similar geometry, velocities, and kinematic viscosities, the two systems are different in several important ways, and only some of these differences are properly approximated with this model.

Firstly, the surface tension coefficient for steel-argon is more than 16 times of that of the water-air. This property and others used in preliminary calculations are listed in Table II. Secondly, the static contact angle, $\theta_o$, in the liquid steel-argon-ceramic system is

150° [39], which indicates much less wettability than the $\theta_o$ of 50° in the air-water-plastic system. Unfortunately, the other contact angles needed in Eq. (6) have not been measured, so Eq. (7) was used as a reasonable first estimate $f_\theta$ for both systems. Thirdly, non-wetting of the liquid metal on the ceramic wall encourages the forming bubble to spread more over the wall, relative to aqueous systems.[12, 14, 20] This might lead to a larger elongation factor, and consequently larger bubbles. Lacking data, however, Eq. (4) was used to calculate $e_d$ in both systems. Fourthly, temperature differences exist in the steel – argon system. However, measurements [14] and calculations [40] both show that gas injected through the "hot" ceramic wall heats up to 99% of the liquid steel temperature even before it hits the liquid steel. Thus, the argon gas injection flow rate used in the model is the "hot" argon flow rate. Finally, the gas is not always injected into a region of stable, fully-developed vertical liquid flow, which is assumed in this work.

Preliminary predictions with the analytical model using these uncertain assumptions are presented in Figure 18, which show the effects of gas injection flow rate and vertical liquid velocity on the predicted bubble diameters for both the steel-argon and water-air systems. Gas density and gas injection hole diameter are predicted to have negligible effect on bubble size in either system.

For the same conditions, argon bubbles generated in liquid steel are predicted to be larger than air bubbles in water. This is due to the higher liquid density and surface tension. During the expansion stage (I), the surface tension force increases by more than double the increase in the drag force, so the force balance of Eq. (15) is satisfied at a larger bubble size $r_e$, compared with the water-air system. At higher liquid velocity, the drag force due to the flowing liquid becomes so dominant that the increase in surface

tension becomes less important. Thus, the difference in bubble sizes between the two systems decreases when liquid velocity is high, and perhaps also when gas flow rate is high.

For the practical range of liquid velocities found in tundish nozzles (0.7 - 1.2m/s), the difference in bubble size between the two systems may sometimes be significant. For example, a typical tundish nozzle with 140 drilled holes and 7 SLPM argon injection has 3.5 ml/s hot argon flow rate through each hole. At a mean liquid velocity of 0.7m/s, argon bubbles in liquid steel are estimated to have about 1.5 times larger diameters than air bubbles in water. The corresponding argon bubble volumes are 3.4 times larger, which is similar to previous calculations [12, 14] in stagnant systems.

Figure 18 shows how the bubble diameter increases sharply with decreasing liquid velocity, for a fixed gas flow rate. In fact, the model breaks down and predicts infinite bubble sizes for U<0.5m/s (water-air) and U<0.7m/s (steel-argon) [35]. This happens because the downward drag force at very low velocity is never able to balance the upward surface tension and buoyancy forces, so bubble size is determined by other phenomena. Physically, the gas flow may break up into large, unstable volumes, with some bubbles rising upwards. To avoid this condition, gas should not be injected into regions of low liquid velocity, such as recirculation zones.

In a real nozzle with hundreds of pierced holes or thousands of tiny refractory pores, a continuous gas curtain might be expected on the gas injection section of the inner wall of the nozzle for mode III. Moreover, the argon gas injected into the liquid steel has a much greater tendency to spread into a gas curtain over the refractory wall, due to the much larger surface tension of the liquid steel and the non-wetting behavior of the liquid

steel on the refractory material. This makes the bubble formation mode more likely to fall into Mode III or IV at a lower liquid velocity than in the water-air system. In addition, the bubbles may subsequently break up and / or coalesce. These phenomena, combined with the difficulty of measuring the required data in molten metal, make the prediction of argon bubble sizes exiting a tundish nozzle for molten steel a very difficult task that needs much further work.

## VIII. SUMMARY

The initial stages of bubble formation from one or two horizontal holes injecting gas into a shearing downward turbulent liquid flow are studied with water experiments and mathematical models. High-speed photography was used to quantify the contact angles, bubble elongation length, mode of bubble formation, bubble size, and size distribution for a wide range of conditions, approximating those in a tundish nozzle used in continuous casting of steel. Bubble formation falls into one of four different modes, which depend primarily on the velocity of the flowing liquid and secondarily on the gas flow rate. In Mode I (low liquid speed and small gas flow rate), uniform-sized bubbles form and detach from the wall. In Mode III (high liquid speed), the injected gas elongates down along the wall and breaks into uneven sized bubbles. Mode II is intermediate between Mode I and Mode III. In Mode IV (high liquid speed and high gas flow rate), the gas elongates a long distance down the nozzle walls, forming a sheet before breaking up.

An analytical two-stage model is developed to predict the mean bubble size for non-mode IV flow conditions, with internal parameters taken solely from measurements. The predictions agree well with the measured sizes and both show the following trends:

- The mean bubble size increases with increasing gas injection flow rate.
- The mean bubble size increases with decreasing shearing liquid velocity.
- The mean bubble size in flowing liquid is significantly smaller than in stagnant liquid.
- The mean bubble size is relatively independent of gas injection hole size, especially at high liquid velocity.
- The gas composition has little influence on bubble size.

Preliminary predictions of argon bubbles generated in the liquid steel in a tundish nozzle using uncertain data suggest the following:

- It is possible to use Mode IV flow to prevent liquid contact with the wall, and thereby avoiding inclusion buildup and clogging. However, the gas injection rates are prohibitively high and other flow-related problems are likely.
- Compared to the water-air system, argon bubbles in liquid steel should tend to spread more over the ceramic nozzle wall in liquid steel and fall into Mode II or III. Thus, the argon bubbles likely have a larger tendency to have non-uniform sizes when detaching from the wall.
- Argon bubbles generated in liquid steel should be larger than air bubbles in water for the same flow conditions. The difference should become more significant at lower liquid velocity and smaller gas injection flow rate.

Finally, a preliminary numerical simulation with a VOF model shows qualitative agreement with experimental observations of the bubble formation sequence, but more work is needed for a quantitative match.

## ACKNOWLEDGMENTS

The authors wish to thank the Continuous Casting Consortium at UIUC, including Allegheny Ludlum, (Brackenridge, PA), Armco Inc. (Middletown, OH), Columbus Stainless (South Africa), Inland Steel Corp. (East Chicago, IN), LTV Steel (Cleveland, OH), and Stollberg, Inc., (Niagara Falls, NY) for their continued support of our research. Final thanks are extended to Professor J. Mazumder (U. Michigan) for use of the high-speed video camera, and Flow Science, Inc. for FLOW-3D.

## NOMENCLATURE

| | |
|---|---|
| $D$ | instantaneous equivalent bubble diameter (mm) |
| $D_N$ | diameter of nozzle bore (mm) |
| $d$ | gas injection hole diameter (mm) |
| $_d$ | subscript referring to instant of detachment, stage 2 |
| $e$ | elongation factor (=L/D) |
| $_e$ | subscript referring to end of expansion, stage 1 |
| $F_B$ | buoyancy force for a bubble (N) |
| $F_D$ | drag force acting on bubble from flowing liquid (N) |
| $F_S$ | surface tension force on bubble (N) |
| $F_{Sz}$ | vertical component of surface tension force on bubble (N) |

| | |
|---|---|
| $f$ | frequency of bubble formation ($s^{-1}$) |
| $f_\theta$ | contact angle function, $f_\theta = sin\theta_O(cos\theta_r - cos\theta_a)$ |
| $L$ | elongation length at instant of detachment ($=e_d D_d$) (mm) |
| $P_b$ | pressure in bubble (Pa) |
| $P_g$ | gas injection pressure in Eq. (28) (Pa) |
| $Q_g$ | gas injection flow rate per hole (ml/s) |
| $r$ | horizontal radius of an ellipsoidal bubble (mm) |
| $Re_{bub}$ | Reynolds number of bubble ($=uD/\upsilon$) |
| $t$ | time during bubble formation (s) |
| $U$ | average liquid velocity in nozzle (m/s) |
| $u$ | liquid velocity profile across nozzle bore =u(y) (m/s) |
| $\bar{u}$ | average liquid velocity across bubble (m/s) |
| $V_b$ | bubble volume ($=\pi D^3/6$) (ml) |
| $y, z$ | horizontal and vertical coordinate directions (m) |
| $\mu_g$, $\mu_l$ | molecular viscosity of gas and liquid (kg/m-s) |
| $\theta_o$ | static contact angle ( °) |
| $\theta_a$, $\theta_r$ | advancing and receding contact angles of a forming bubble ( °) |
| $\rho_g$, $\rho_l$ | density of gas and liquid ($kg/m^3$) |
| $\sigma$ | liquid surface tension (N/m) |
| $\upsilon$ | kinematic viscosity of liquid $=(\mu_l/\rho_l)$ ($m^2/s$) |

## REFERENCES

1. N. Bessho, R. Yoda, T. Yamasaki, T. Fuji, T. Nozaki and S. Takatori: "Numerical Analysis of Fluid Flow in the Continuous Casting Mold by a Bubble Dispersion

Model", *Transactions of the ISS (Iron and Steelmaker),* 1991, vol. 18 (4), pp. 39-44.

2. B.G. Thomas and X. Huang: "Effect of Argon Gas on Fluid Flow in a Continuous Slab Casting Mold", *76th Steelmaking Conference*, Dallas, TX, Iron and Steel Society, Warrendale, PA, 1993, vol. 76, pp. 273-89.

3. B.G. Thomas, X. Huang and R.C. Sussman: "Simulation of Argon Gas Flow Effects in a Continuous Slab Caster", *Metallurgical Transactions B,* 1994, vol. 25B (4), pp. 527-47.

4. B.G. Thomas, A. Dennisov and H. Bai: "Behavior of Argon Bubbles during Continuous Casting of Steel", *80th ISS Steelmaking Conference*, Chicago, 1997, pp. 375-84.

5. J. Knoepke and M. Hubbard: "Pencil Blister Reductions at Inland Steel Company", *77th Steelmaking Conference*, Washington, D. C, 1994, pp. 381-88.

6. L. Wang, H.-G. Lee and P. Hayes: "Prediction of the Optimum Bubble Size for Inclusion Removal from Molten Steel by Flotation", *ISIJ International,* 1996, vol. 36 (1), pp. 7-16.

7. K. Tabata, T. Kakehi and M. Terao: *Gas Injection Methods at Tundish Slide Gate Valve for Continuous Casting*, Shinagawa Technical Report, Report No. 31, 1988.

8. M. Sano and K. Mori: "Bubble Formation from Single Nozzles in Liquid Metals", *Trans. JIM,* 1976, vol. 17, pp. 344-52.

9. A. Thomas, S. Tu and D. Janke: "Frequency of Bubble Formation in Water and Liquid Iron", *Steel Research,* 1997, vol. 68 (5), pp. 198-200.

10. M. Sano, Y. Fujita and K. Mori: "Formation of Bubbles at Single Nonwetted Nozzles in Mercury", *Metallurgical Transactions B,* 1976, vol. 7B (June), pp. 300-01.

11. M. Iguchi, H. Kawabata, K. Nakajima and Z. Morita: *Metallurgical Transactions B,* 1995, vol. 26B, p. 67.

12. G.A. Irons and R.I.L. Guthrie: "Bubble Formation at Nozzles in Pig Iron", *Metallurgical Transactions B,* 1978, vol. 9B (March), pp. 101-10.

13. K.G. Davis, G.A. Irons and R.I.L. Guthrie: "X-Ray Cinematographic Observations of Gas Injection into Liquid Metals", *Metallurgical Transactions B,* 1978, vol. 9B (December), pp. 721-22.

14. M. Iguchi, T. Chihara, N. Takanashi, Y. Ogawa, N. Tokumitsu and Z. Morita: "X-ray Fluoroscopic Observation of Bubble Characteristics in a Molten Iron Bath", *ISIJ International,* 1995, vol. 35 (11), pp. 1354-61.

15. R.I.L. Guthrie: *Engineering in Process Metallurgy*, Clarendon Press, Oxford, UK, 1992, p. 457.

16. R. Kumar and N.R. Kuloor: "The Formation of Bubbles and Drops", in *Advances in Chemical Engineering*, vol. 8, Academic Press, New York, London, 1970, pp. 255-368.

17. R. Clift, J.R. Grace and M.E. Weber: *Bubbles, Drops, and Particles*, Academic Press Inc., New York, 1978.

18. H. Tsuge: "Hydrodynamics of Bubble Formation from Submerged Orifices", in *Encyclopedia of Fluid Mechanics*, vol. 3, Gulf Publishing Co., Houston, TX, 1986, pp. 191-232.

19. N. Rabiger and A. Vogelpohl: "Bubble Formation and its Movement in Newtonian and Non-Newtonian Liquid", in *Encyclopedia of Fluid Mechanics*, vol. 3, Gulf Publishing Co., Houston, TX, 1986, pp. 58-88.

20. Z. Wang, K. Mukai and D. Izu: "Influence of Wettability on the Behavior of Argon Bubbles and Fluid Flow inside the Nozzle and Mold", *ISIJ International,* 1999, vol. 39 (2), pp. 154-63.

21. J.F. Davidson and B.O.G. Schuler: "Bubble Formation at an Orifice in an Inviscid Liquid", *Trans. Instn Chem. Engrs,* 1960, vol. 38, pp. 335-42.

22. R. Kumar and N.R. Kuloor: *Chem. Tech.,* 1967, vol. 19, p. 733.

23. W.V. Pinczewski: "The Formation and Growth of Bubbles at a Submerged Orifice", *Chemical Engineering Science,* 1981, vol. 36, pp. 405-11.

24. K. Terasaka and H. Tsuge: "Bubble Formation at a Single Orifice in Highly Viscous Liquids", *Journal of Chemical Engineering of Japan,* 1990, vol. 23 (2), pp. 160-65.

25. K. Terasaka and H. Tsuge: "Bubble Formation under Constant-Flow Conditions", *Chemical Engineering Science,* 1993, vol. 48 (19), pp. 3417-22.

26. H. Tsuge, Y. Nakajima and K. Terasaka: "Behavior of Bubble Formed from a Submerged Orifice under High System Pressure", *Chemical Engineering Science,* 1992, vol. 47 (13/14), pp. 3273-80.

27. T. Hong, C. Zhu and L.-S. Fan: "Numerical Modeling of Formation of Single Bubble Chain and Bubble Breakage due to Collision with Particle in Liquid", *1996 ASME Fluids Division Conference*, 1996, vol. FED 236, pp. 581-88.

28. C.W. Hirt and B.D. Nichols: "Volume of Fluid (VOF) Method for the Dynamics of Free Boundary", *Journal of Computational Physics,* 1981, vol. 39, pp. 201-25.

29. S.C. Chuang and V.W. Goldschmidt: "Bubble Formation due to a Submerged Capillary Tube in Quiescent and Coflowing Streams", *Journal of Basic Engineering,* 1970, vol. 92, pp. 705-11.

30. Y. Kawase and J.J. Ulbrecht: "Formation of Drops and Bubbles in Flowing Liquids", *Ind. Eng. Chem. Process Des. Dev.,* 1981, vol. 20 (4), pp. 636-40.

31. I.B.V. Morgenstern and A. Mersmann: "Aeration of Highly Viscous Liquids", *Germany Chemical Engineering,* 1982, vol. 5, pp. 374-79.

32. M. Burty, M. Larrecq, C. Pusse and Y. Zbaczyniak: "Experimental and Theoretical Analysis of Gas and Metal Flows in Submerged Entry Nozzles in Continuous Casting", *13th PTD Conference*, Nashville, TN, 1995, vol. 13, pp. 287-92.

33. R.H.S. Winterton: "Sizes of Bubbles Produced by Dissolved Gas Coming out of Solution on the Walls of Pipes in Flowing Systems", *Chemical Engineering Science,* 1972, vol. 27, pp. 1223-30.

34. R.H.F. Pao: *Fluid Dynamics*, Merrill, New York, 1967.

35. H. Bai: *Argon Bubble Behavior in Slide-Gate Nozzles during Continuous Casting of Steel Slabs*, Ph.D. Thesis, University of Illinois at Urbana-Champaign, 2000.

36. S.L. Soo: *Multiphase Fluid Dynamics*, Science Press, Gower, Beijing, 1990.

37. B.E. Launder and D.B. Spalding: "Numerical Computation of Turbulent Flows", *Comp. Meth. Applied Mechanics and Engr.,* 1974, vol. 13, pp. 269-89.

38. Flow Science Inc.: *FLOW-3D User's Manual*, Los Alamos, NM, 1997.

39. L. Jimbo, A. Sharan and A.W. Cramb: "Recent measurements of surface and interfacial tensions in steels", *76th SteelMaking Conference*, Dallas, TX, 1993, pp. 485-94.

40. H. Bai and B.G. Thomas: "Turbulent Flow of Liquid Steel and Argon Bubbles in Slide-Gate Tundish Nozzles, Part I: Model Development and Validation", *Metallurgical and Materials Transactions B,* 2001, vol. 32B.

## FIGURE AND TABLE CAPTIONS

Table I Average contact angles measured in the water experiments

Table II Physical properties and operating conditions used in the two-stage model

Figure 1 Schematic of water experiment for bubble formation study

Figure 2 Measured air bubble sizes in stagnant water compared with Iguchi's empirical correlation

Figure 3 Effect of gas injection rate and water velocity on modes and measured bubble sizes (mean equivalent sphere diameter) and size range (a) 0.2mm injection hole diameter (b) 0.3mm injection hole diameter (c) 0.4mm injection hole diameter

Figure 4 Mean air bubble volumes measured in stagnant and flowing water

Figure 5 Effect of gas composition, gas flow rate and liquid velocity on measured bubble size

Figure 6 Figure 6 Example experiment photographs and schematics showing the four different bubble formation modes (a) Mode I, side view (b) Mode II, side view (c) Mode III, side view (d) Mode IV, side view (e) Mode I, end view (f) traced schematic of Mode I, end view (g) traced schematic of Mode III, end view (h) Mode III, end view (i) Mode IV, end view

Figure 7 Photograph series showing the bubble formation process for Mode I and Mode III (a) Mode I -U=0.9m/s, $Q_G$=0.5ml/s, d=0.4mm, Bubble frequency f=293/s, Equivalent bubble diameter: measured: 1.51mm, predicted: 1.53mm (b) Mode III - U=1.9m/s, $Q_G$=1.86ml/s, d=0.3mm, Bubble frequency f=444/s, Equivalent bubble diameter: measured: 2.0mm, predicted:1.95mm

Figure 8 Bubble formation sequence traced from Figure 7 (a) Mode I (b) Mode III

Figure 9 Bubble elongation length measured at instant of bubble detachment from the gas injection hole (a) Schematic of the measurement (b) Measured elongation (*L*)

Figure 10 Measured and fitted elongation factors at bubble detachment (a) effect of gas injection (b) effect of liquid velocity

Figure 11 Schematic bubble shapes showing advancing and receding contact angles (a) water-air system - measured (b) steel-argon system - expected

Figure 12 Effect of mean liquid velocity on measured and fitted contact angle function

Figure 13 Schematic of liquid velocity profile near wall region and forces acting on a growing bubble

Figure 14 Evolution of estimated vertical forces acting on a bubble growing in water

Figure 15 Idealized sequence of bubble formation in the two stage model (a) expansion stage (b) elongation stage

Figure 16 Comparison of measured and predicted air bubble sizes in water for different gas flow rates, liquid velocities, and injection hole sizes (a) U=0.9m/s (b) U=1.4m/s (c) U=1.9m/s (d) U=2.5m/s

Figure 17 Simulated bubble formation sequence calculated using VOF model

Figure 18 Comparison of estimated argon bubble size in liquid steel with air bubble size in water

Table I Average contact angles measured in the water experiments

| Average liquid velocity U (m/s) | Static contact angle $\theta_O$ (°) | Advancing contact angle $\theta_a$ (°) | Receding contact angle $\theta_r$ (°) | Contact angle function $f_\theta = \sin\theta_O(\cos\theta_r-\cos\theta_a)$ |
|---|---|---|---|---|
| 0.9 | 50 | 64 | 35 | 0.30 |
| 1.4 | 50 | 82 | 29 | 0.56 |
| 1.9 | 50 | 101 | 22 | 0.85 |
| 2.5 | 50 | 134 | 17 | 1.26 |

Table II Physical properties and operating conditions used in the two-stage model

| Parameters | Symbol | Unit | Water-air system | Steel-hot argon system |
|---|---|---|---|---|
| Liquid density | $\rho_l$ | $Kg/m^3$ | 1000 | 7021 |
| Gas density | $\rho_g$ | $Kg/m^3$ | 1.29 | 0.27 |
| Liquid viscosity | $\mu_l$ | kg/(ms) | 0.001 | 0.0056 |
| Gas viscosity | $\mu_g$ | kg/(ms) | 1.7E-5 | 7.42E-5 |
| Surface tension coefficient | $\sigma$ | N/m | 0.073 | 1.192 |
| Gas injection flow rate per pore | $Q_g$ | ml/s | 0.1 - 6 ml/s | 0.1 - 6 ml/s |
| Nozzle diameter | $D_n$ | mm | 35 | 78 |
| Diameter of gas injection hole | $d$ | mm | 0.2, 0.3, 0.4 | 0.2, 0.3, 0.4 |
| Average velocity 0of the liquid | $U$ | m/s | 0.9, 1.4, 1.9, 2.5 | 0.7, 0.9, 1.4,1.9, 2.5 |
| Elongation factor at detachment | $e_d$ | | 1.32, 1.53,1.67, 1.76 | Equation 4 |
| Contact angle function $f_\theta=\sin\theta_o(\cos\theta_r-\cos\theta_a)$ | $f_\theta$ | | 0.30, 0.56, 0.85, 1.26 | Equation 7 |

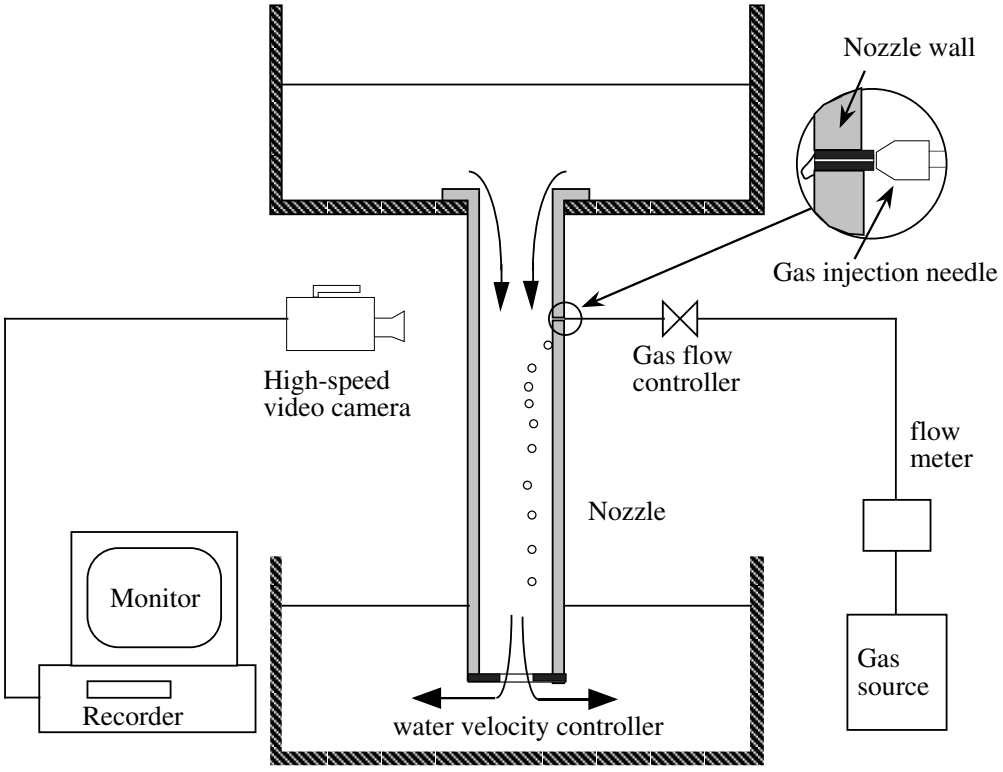


Figure 1 Schematic of water experiment for bubble formation study

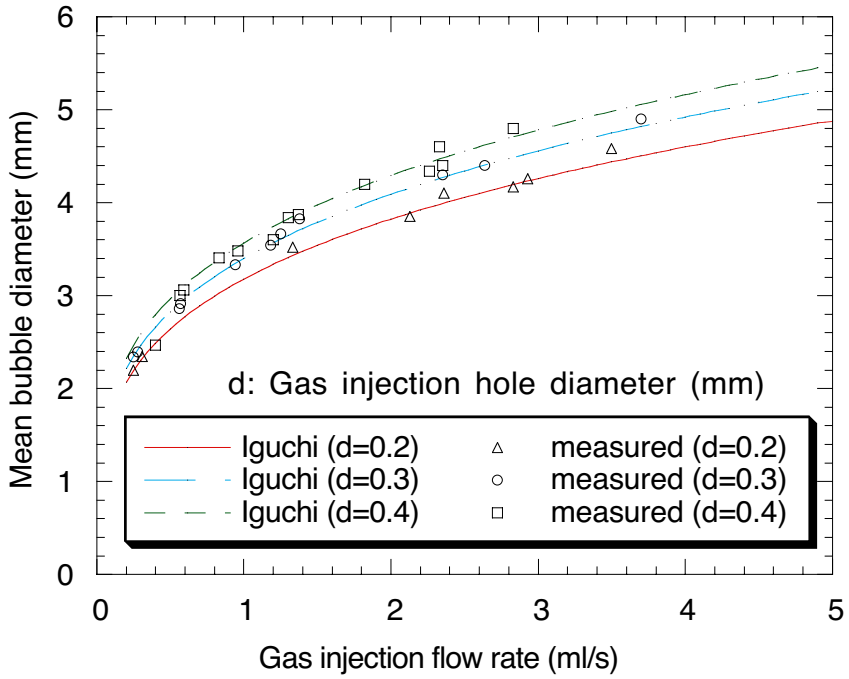


Figure 2 Measured air bubble sizes in stagnant water compared with Iguchi's empirical correlation [34]

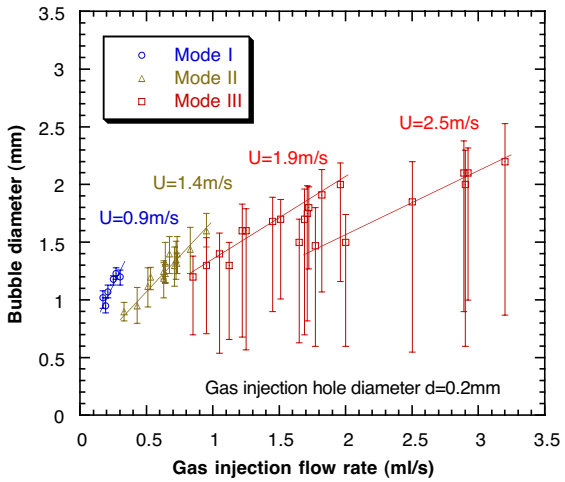


(a)

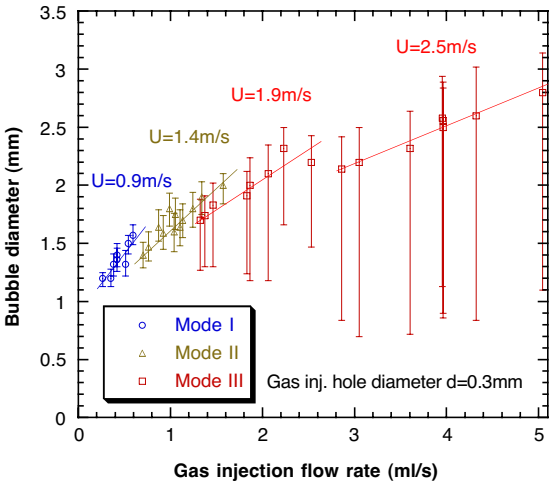


(b)

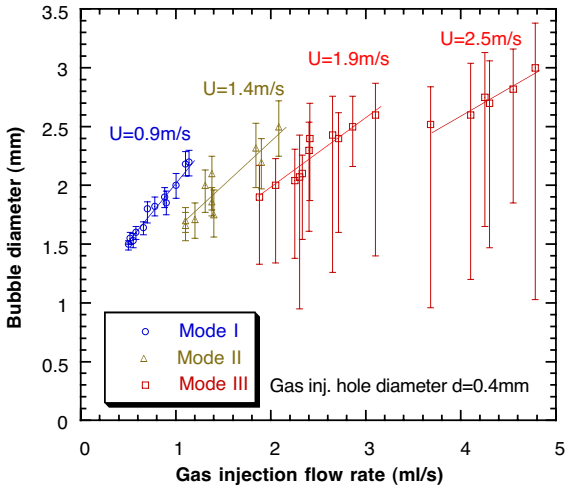


(c)

Figure 3 Effect of gas injection rate and water velocity on modes and measured bubble sizes (mean equivalent sphere diameter) and size range (a) 0.2mm injection hole diameter (b) 0.3mm injection hole diameter (c) 0.4mm injection hole diameter

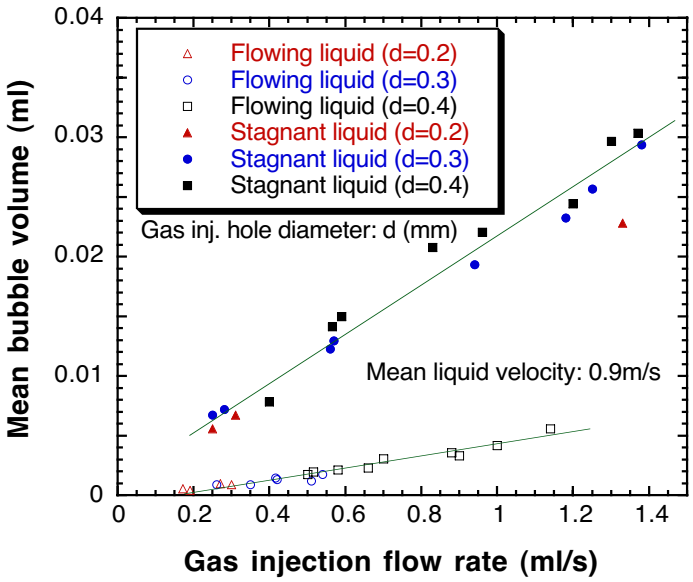


Figure 4 Mean air bubble volumes measured in stagnant and flowing water

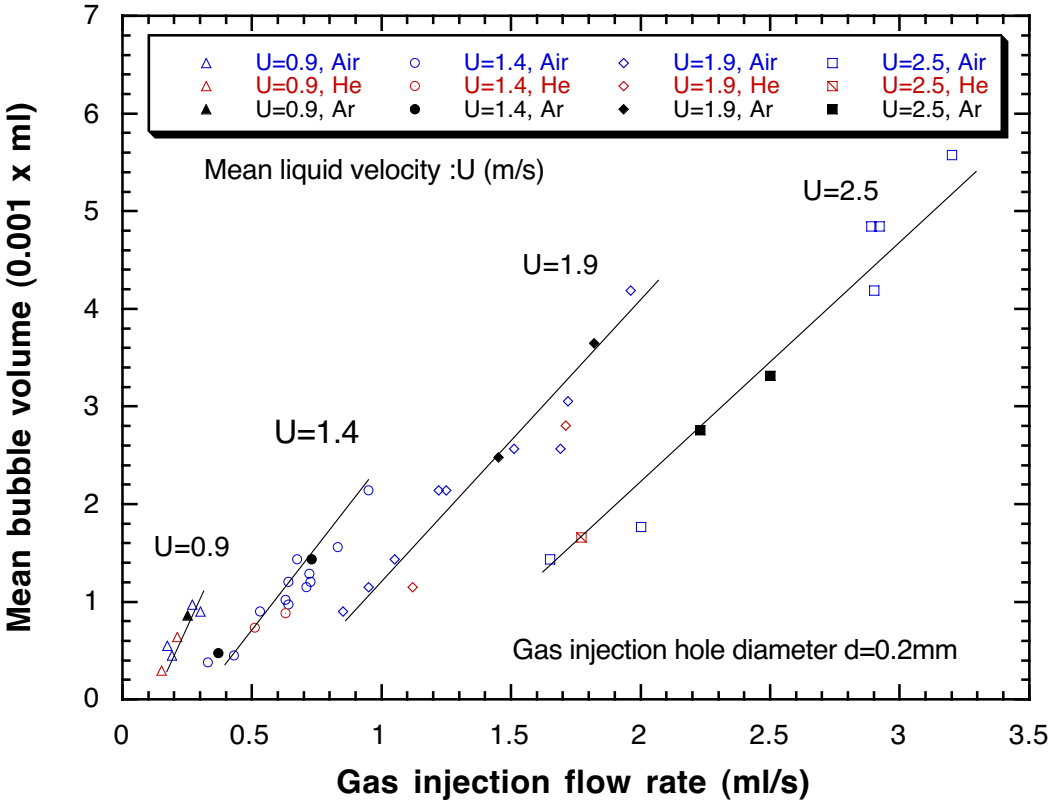


Figure 5 Effect of gas composition, gas flow rate and liquid velocity on measured bubble size

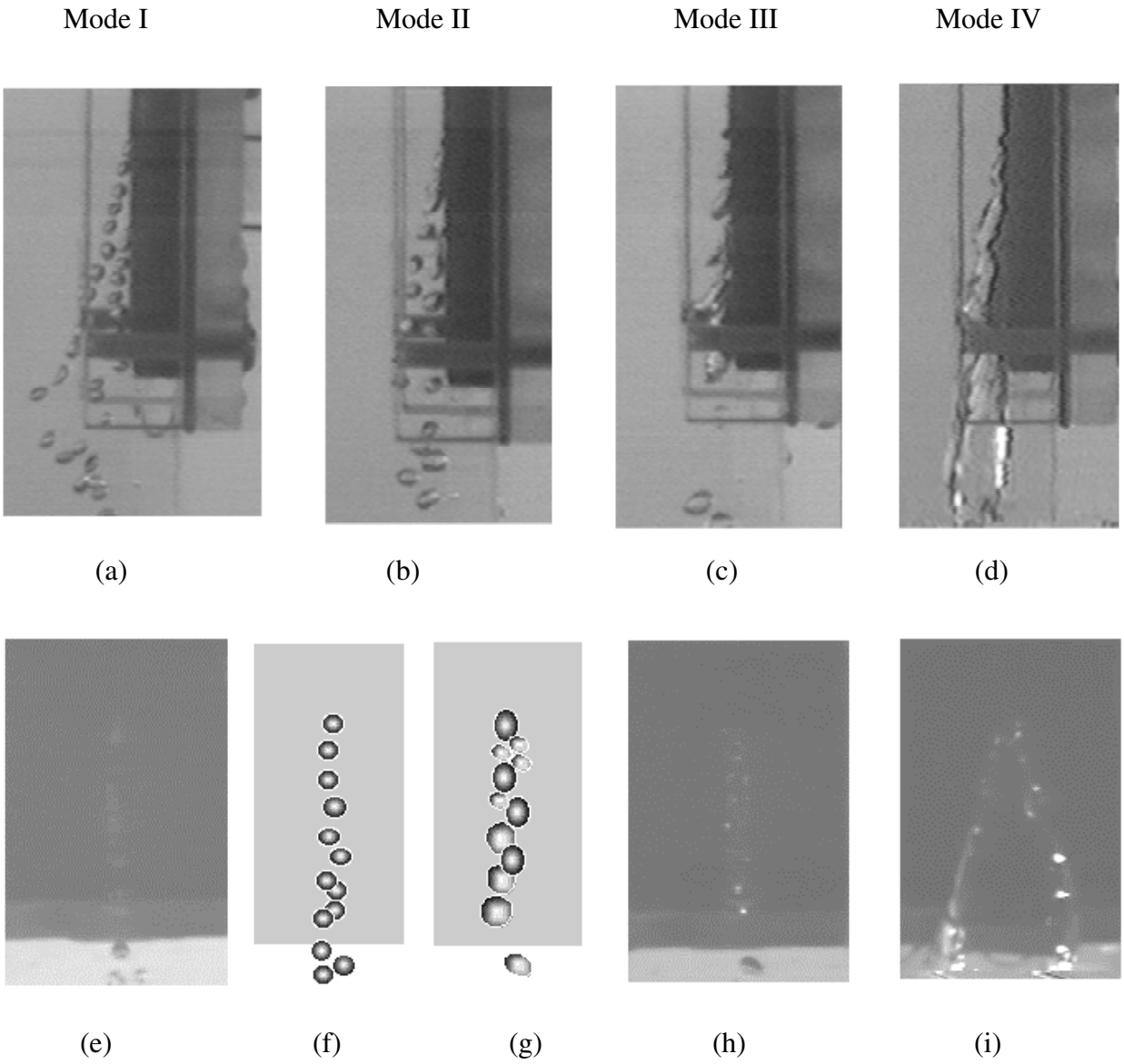


Figure 6 Example experiment photographs and schematics showing the four different bubble formation modes (a) Mode I, side view (b) Mode II, side view (c) Mode III, side view (d) Mode IV, side view (e) Mode I, end view (f) traced schematic of Mode I, end view (g) traced schematic of Mode III, end view (h) Mode III, end view (i) Mode IV, end view

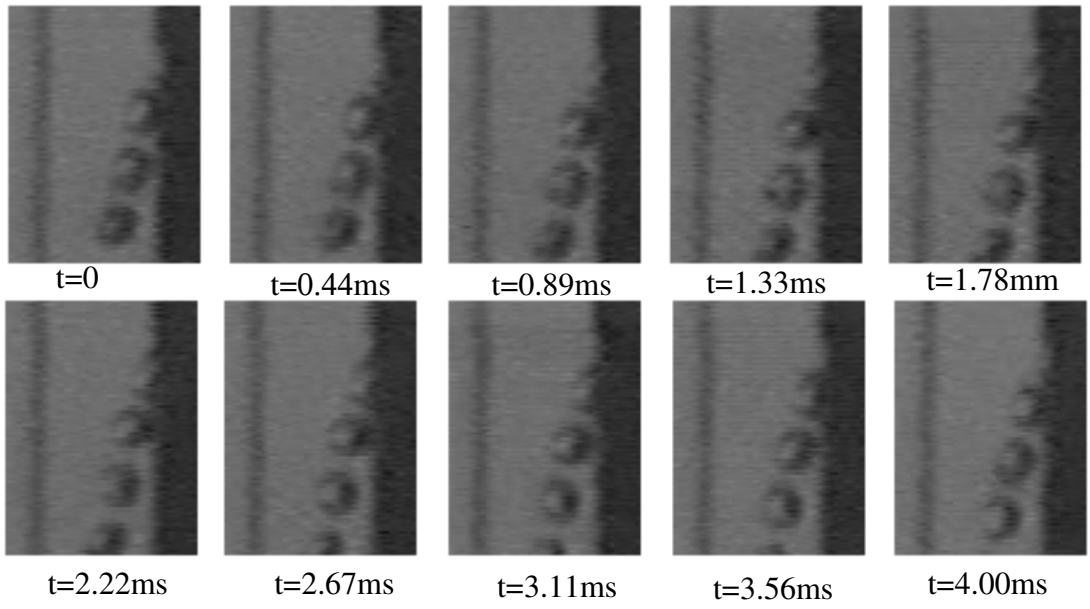


(a)

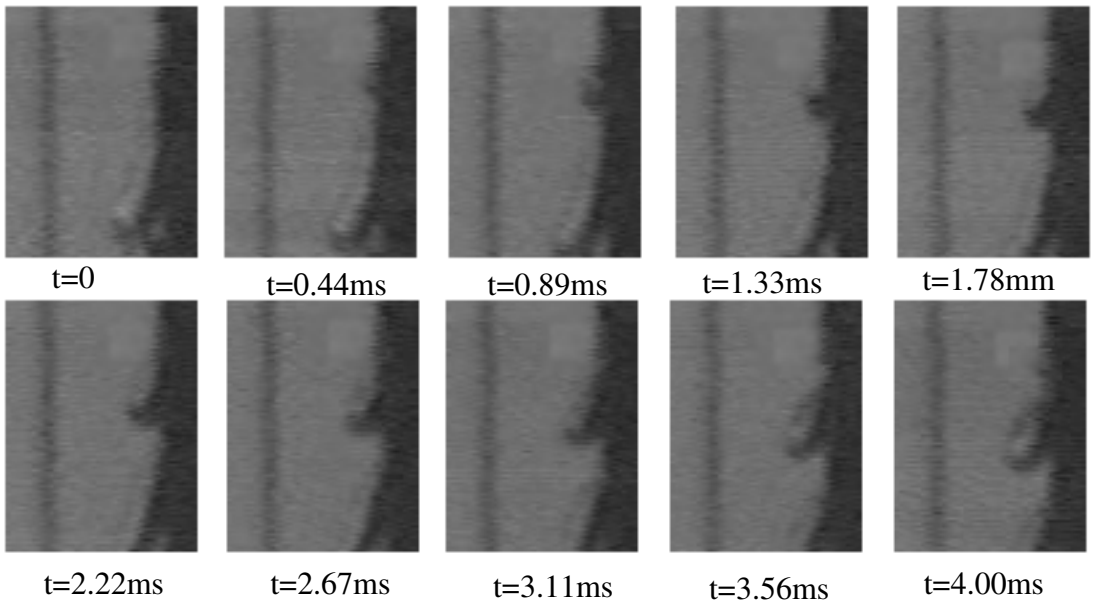


(b)

Figure 7 Photograph series showing the bubble formation process for Mode I and Mode III
(a) Mode I -- U=0.9m/s, $Q_G$=0.5ml/s, d=0.4mm, Bubble frequency f=293/s,
Equivalent bubble diameter: measured: 1.51mm, predicted: 1.53mm
(b) Mode III --U=1.9m/s, $Q_G$=1.86ml/s, d=0.3mm, Bubble frequency f=444/s,
Equivalent bubble diameter: measured: 2.0mm, predicted:1.95mm

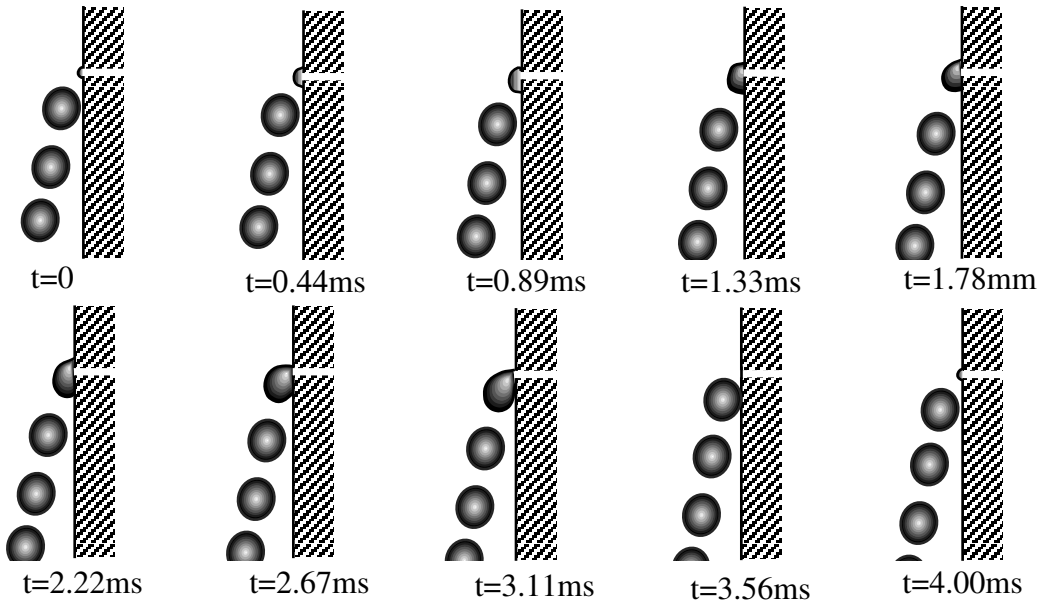


(a)

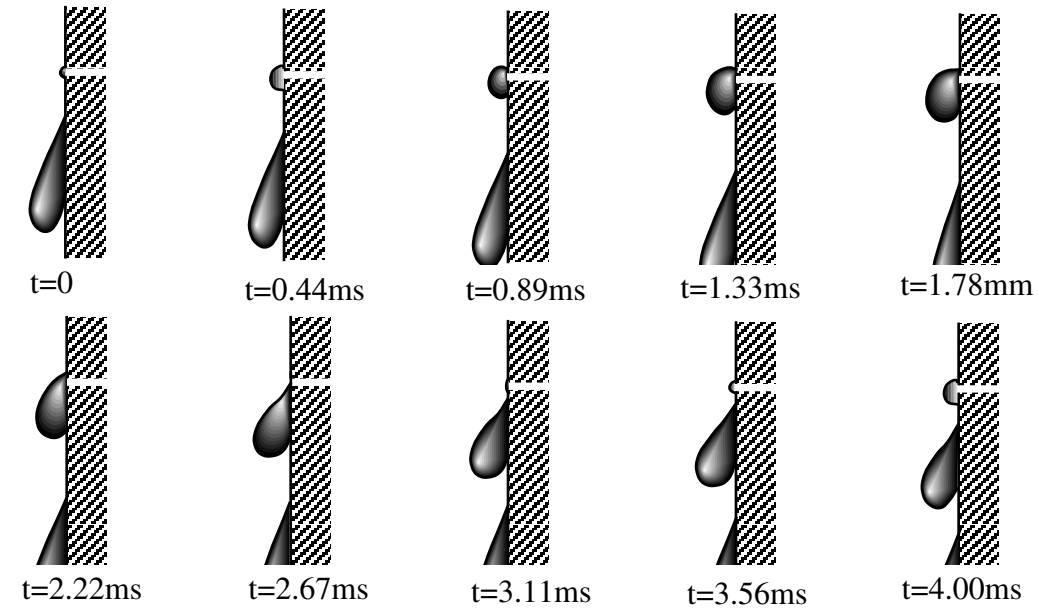


(b)

Figure 8 Bubble formation sequence traced from Figure 7 (a) Mode I (b) Mode III

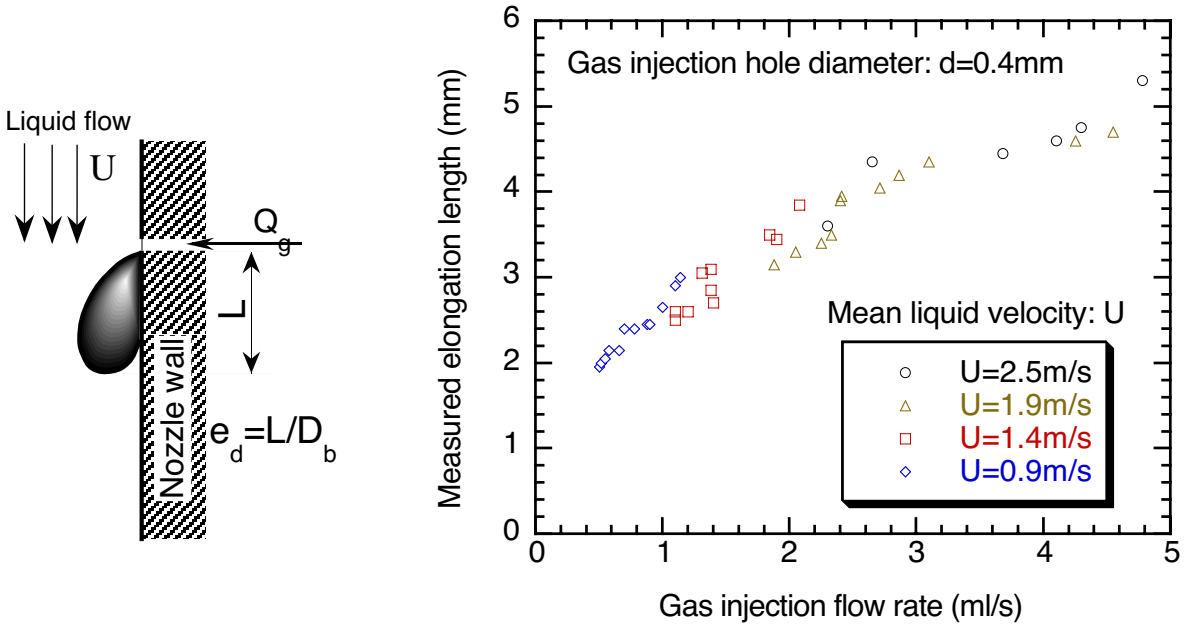


(a) (b)

Figure 9 Bubble elongation length measured at instant of bubble detachment from the gas injection hole (a) Schematic of the measurement (b) Measured elongation ($L$)

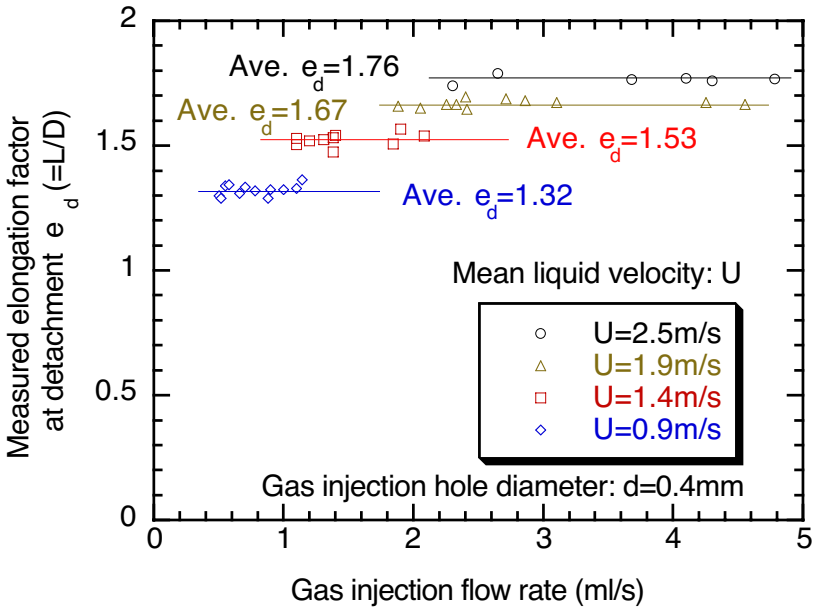


(a)

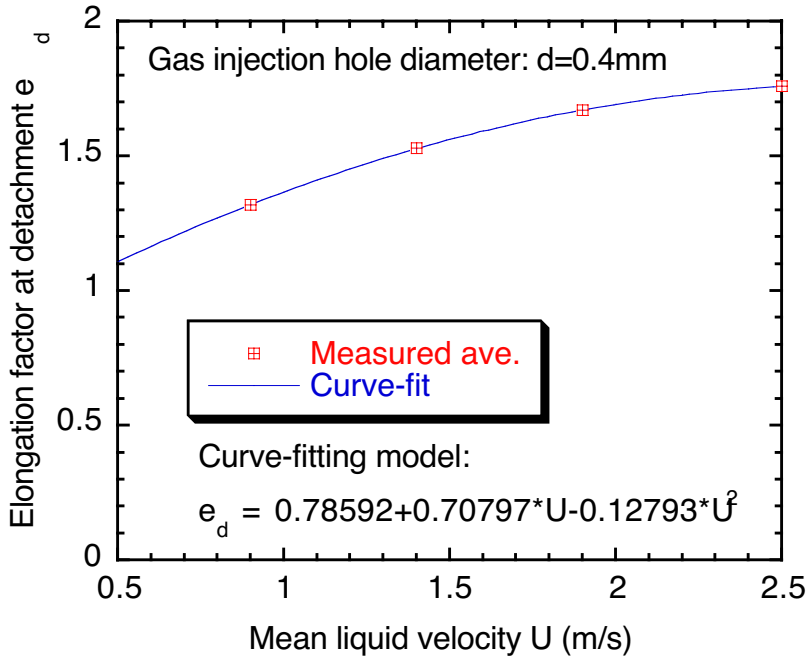


(b)

Figure 10 Measured and fitted elongation factors at bubble detachment (a) effect of gas injection (b) effect of liquid velocity

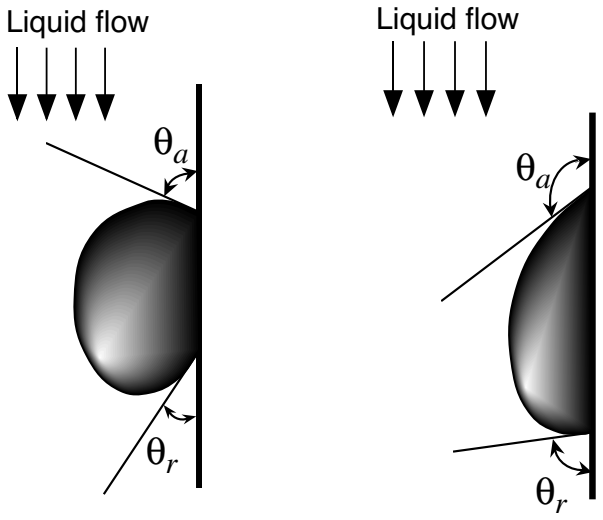


(a) (b)

Figure 11 Schematic bubble shapes showing advancing and receding contact angles (a) water-air system - measured (b) steel-argon system - expected

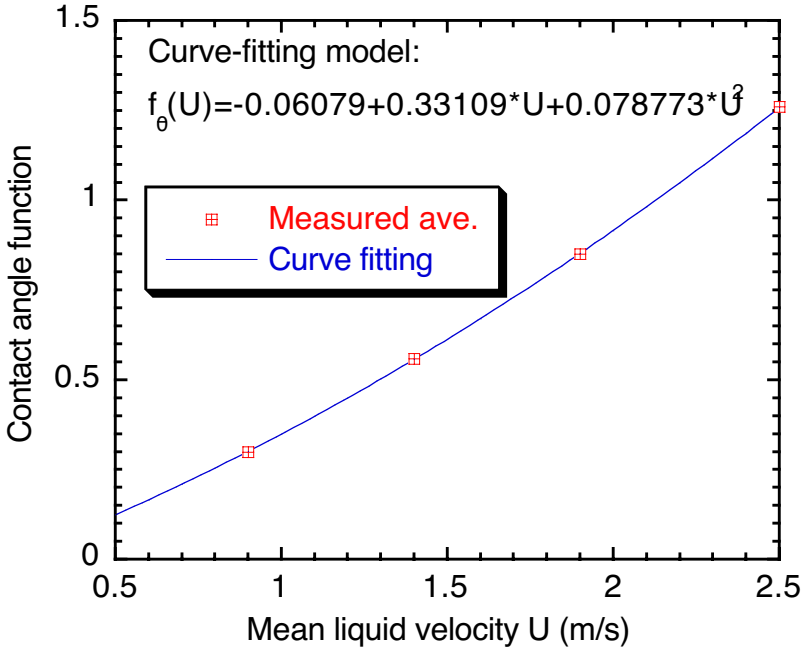


Figure 12 Effect of mean liquid velocity on measured and fitted contact angle function

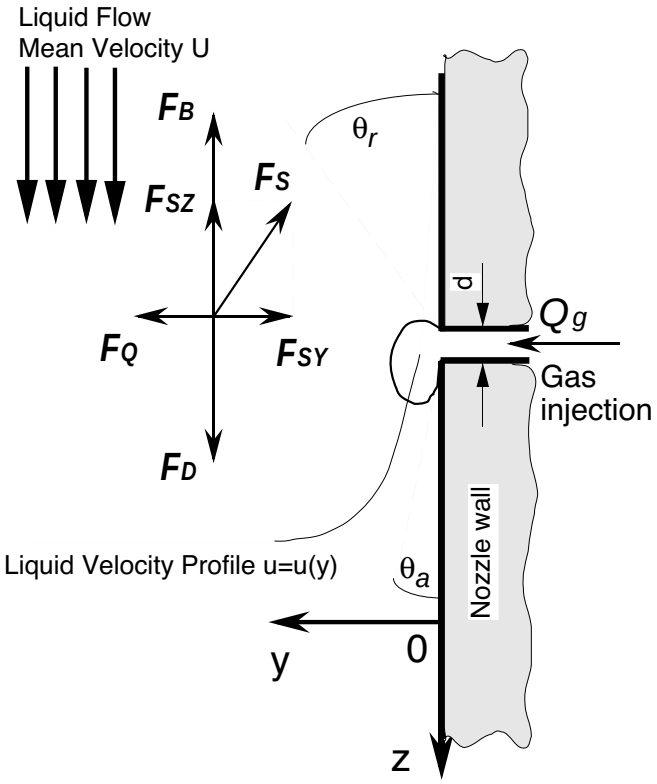


Figure 13 Schematic of liquid velocity profile near wall region and forces acting on a growing bubble

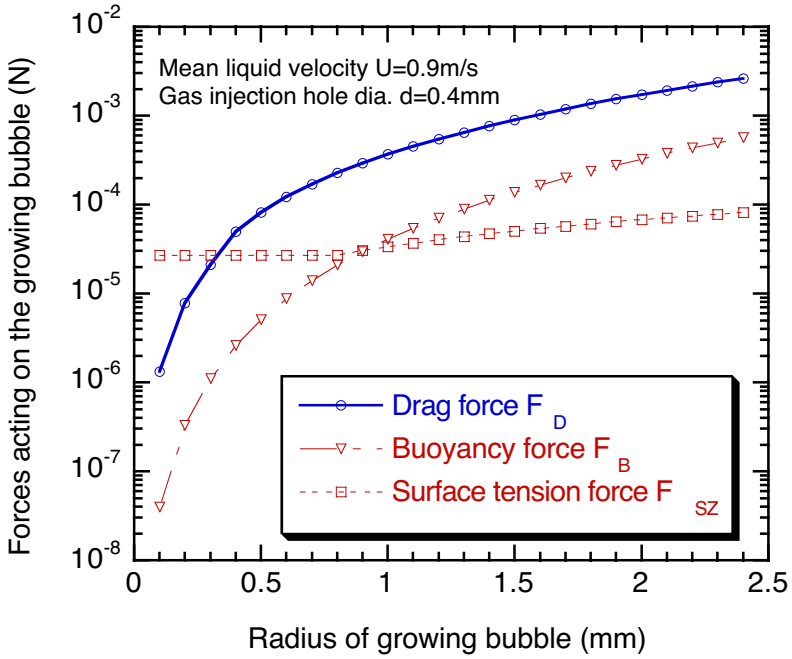


Figure 14 Evolution of estimated vertical forces acting on a bubble growing in water

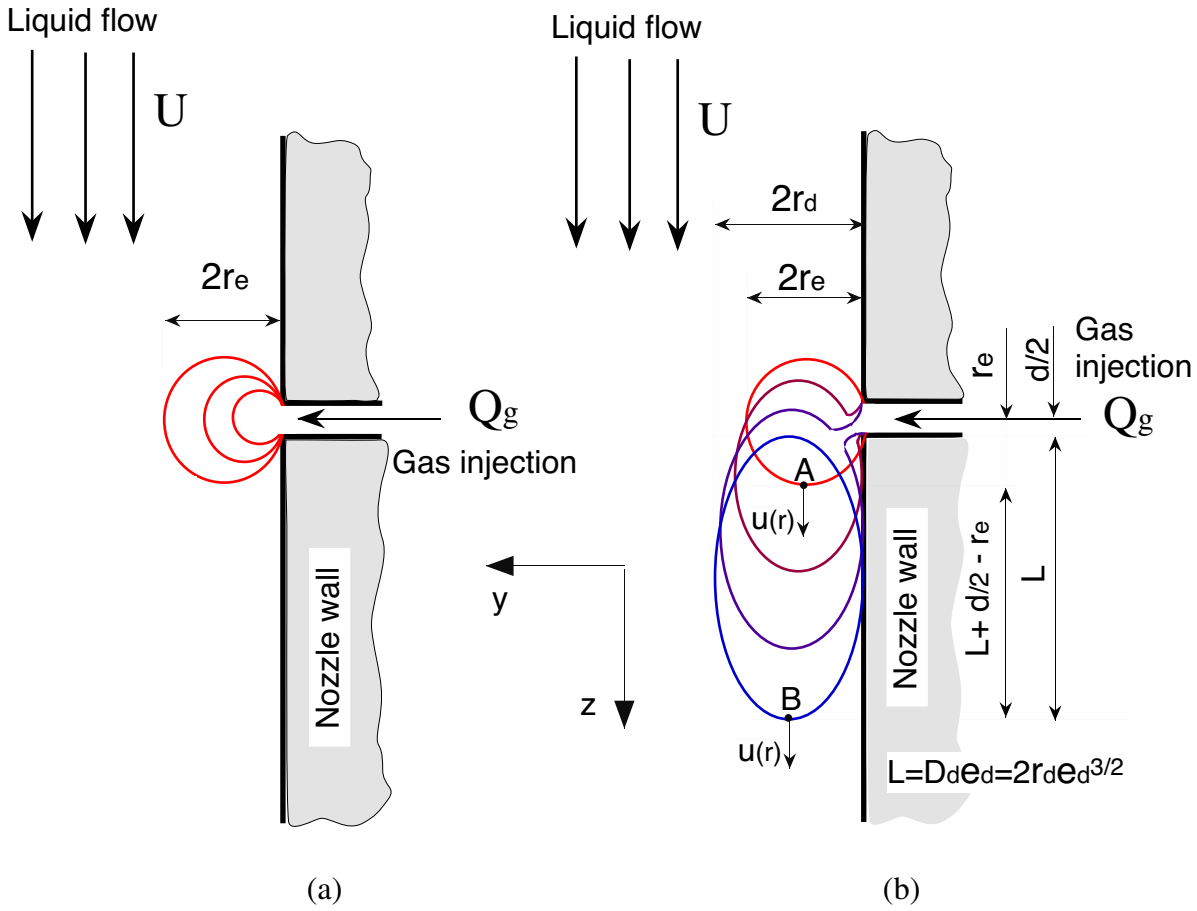


Figure 15 Idealized sequence of bubble formation in the two stage model
(a) expansion stage (b) elongation stage

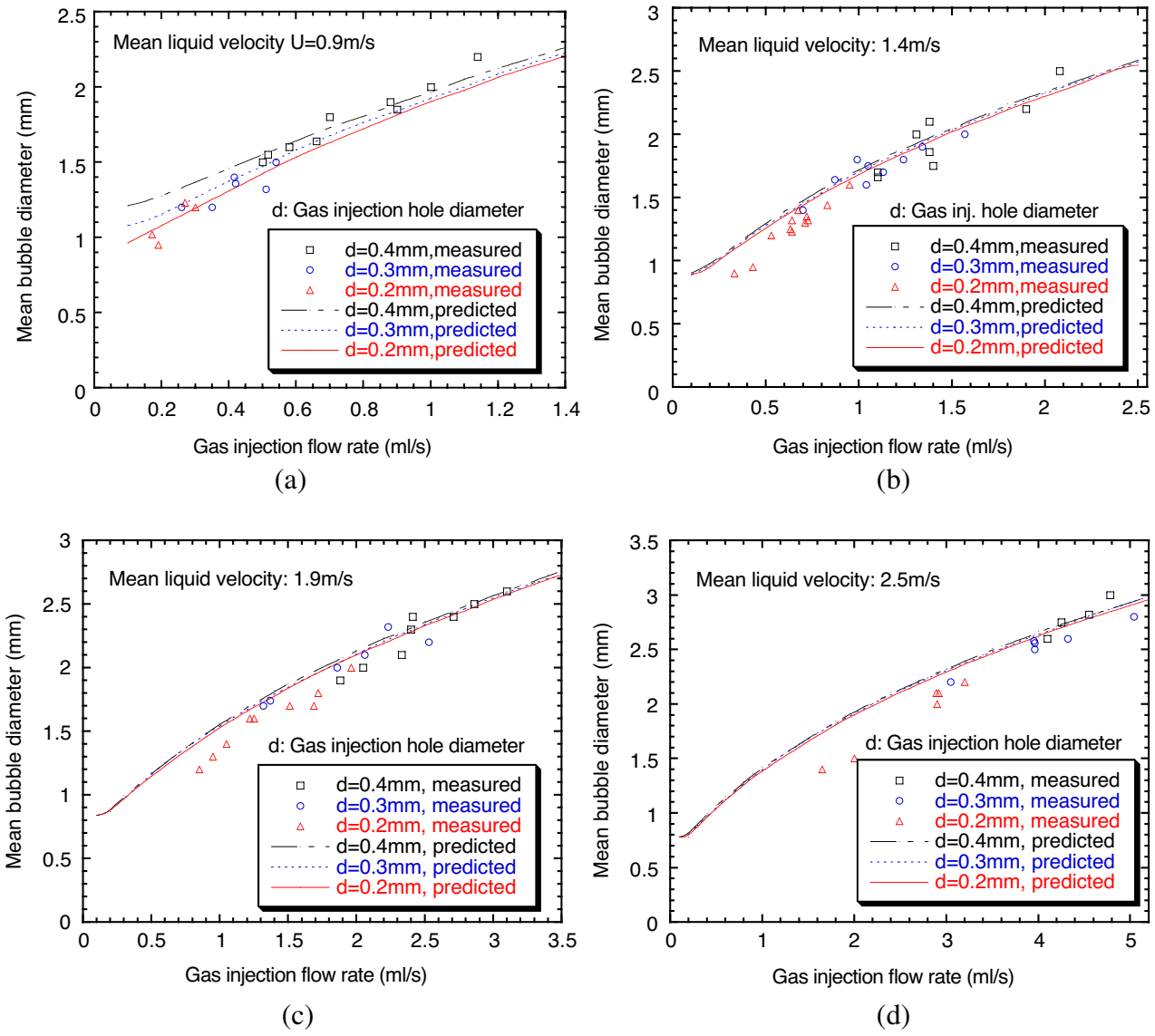


Figure 16 Comparison of measured and predicted air bubble sizes in water for different gas flow rates, liquid velocities, and injection hole sizes
(a) U=0.9m/s (b) U=1.4m/s (c) U=1.9m/s (d) U=2.5m/s

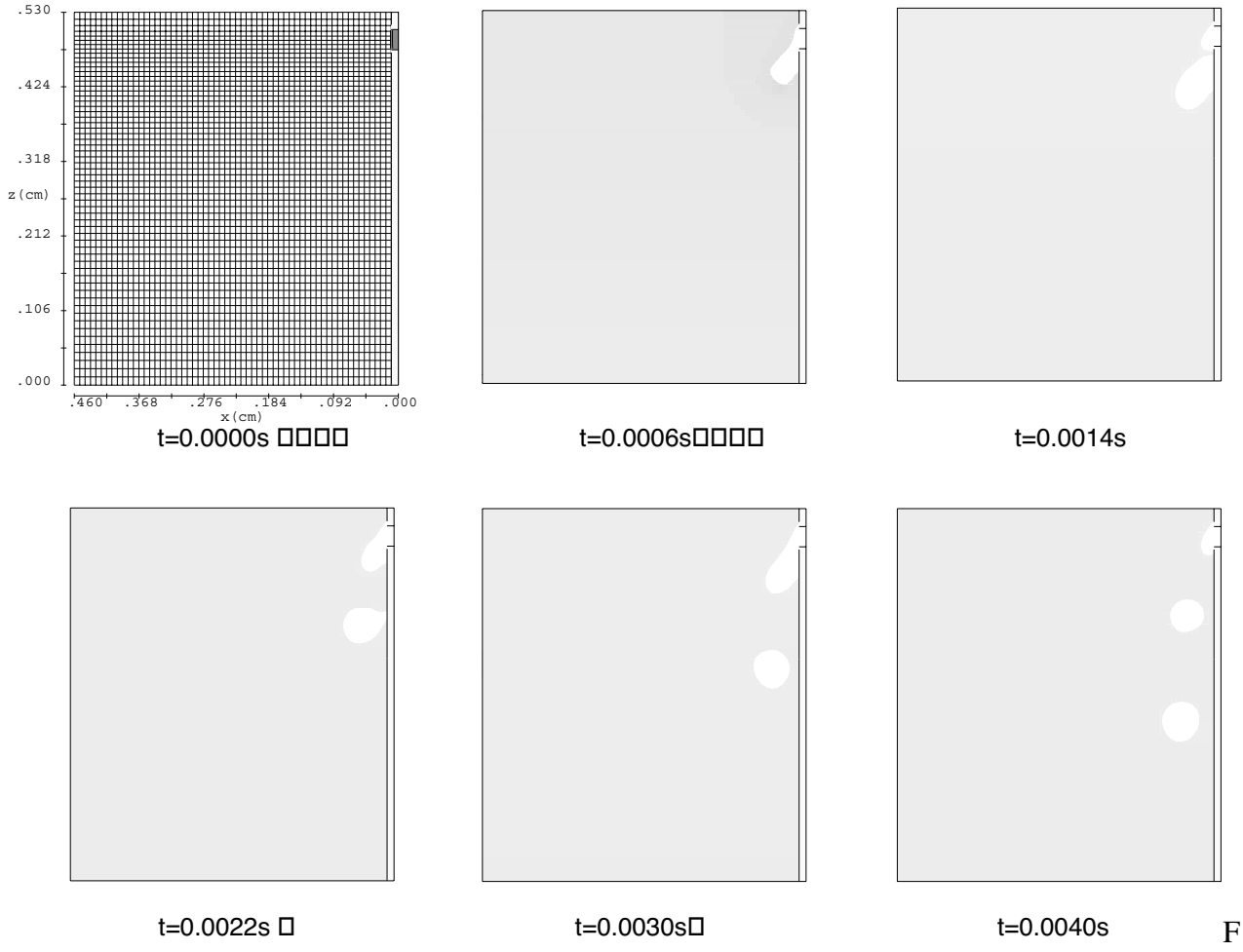


Figure 17 Simulated bubble formation sequence calculated using VOF model

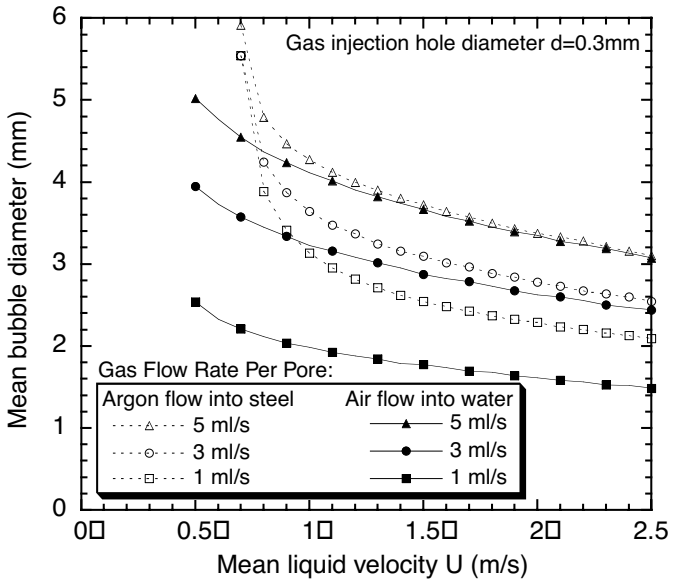


Figure 18 Comparison of estimated argon bubble size in liquid steel with air bubble size in water